CrossMark

The Photon Ring in M87*

Avery E. Broderick[1,2,3], Dominic W. Pesce[4,5], Roman Gold[6], Paul Tiede[1,2,3,4,5], Hung-Yi Pu[7,8,9],
Richard Anantua[4,5,10], Silke Britzen[11], Chiara Ceccobello[12], Koushik Chatterjee[4,5], Yongjun Chen (陈永军)[13,14],
Nicholas S. Conroy[4,15], Geoffrey B. Crew[16], Alejandro Cruz-Osorio[17], Yuzhu Cui (崔玉竹)[18,19,20],
Sheperd S. Doeleman[4,5], Razieh Emami[4], Joseph Farah[21,22], Christian M. Fromm[11,17,23], Peter Galison[5,24,25],
Boris Georgiev[1,2,3], Luis C. Ho (何子山)[26,27], David J. James[28], Britton Jeter[8], Alejandra Jimenez-Rosales[29],
Jun Yi Koay[8], Carsten Kramer[30], Thomas P. Krichbaum[11], Sang-Sung Lee[31,32], Michael Lindqvist[33],
Iván Martí-Vidal[34,35], Karl M. Menten[11], Yosuke Mizuno[17,18,36], James M. Moran[4,5], Monika Moscibrodzka[29],
Antonios Nathanail[17], Joey Neilsen[37], Chunchong Ni[1,2,3], Jongho Park[8,31,48], Vincent Piétu[30], Luciano Rezzolla[17,38,39],
Angelo Ricarte[4,5], Bart Ripperda[40,41], Lijing Shao[11,27], Fumie Tazaki[19], Kenji Toma[42,43], Pablo Torne[11,44],
Jonathan Weintroub[4,5], Maciek Wielgus[11], Feng Yuan (袁峰)[13,45,46], Shan-Shan Zhao[13], and Shuo Zhang[47]

[1] Perimeter Institute for Theoretical Physics, 31 Caroline Street North, Waterloo, ON, N2L 2Y5, Canada; abroderick@perimeterinstitute.ca
[2] Department of Physics and Astronomy, University of Waterloo, 200 University Avenue West, Waterloo, ON, N2L 3G1, Canada
[3] Waterloo Centre for Astrophysics, University of Waterloo, Waterloo, ON, N2L 3G1, Canada
[4] Center for Astrophysics | Harvard & Smithsonian, 60 Garden Street, Cambridge, MA 02138, USA
[5] Black Hole Initiative at Harvard University, 20 Garden Street, Cambridge, MA 02138, USA
[6] CP3 origins | University of Southern Denmark (SDU) Campusvej 55, Odense, Denmark
[7] Department of Physics, National Taiwan Normal University, No. 88, Sec. 4, Tingzhou Road, Taipei 116, Taiwan, R.O.C.
[8] Institute of Astronomy and Astrophysics, Academia Sinica, 11F of Astronomy-Mathematics Building, AS/NTU No. 1, Sec. 4, Roosevelt Road, Taipei 10617, Taiwan, R.O.C.
[9] Physics Division, National Center for Theoretical Sciences, Taipei 10617, Taiwan
[10] Department of Physics & Astronomy, The University of Texas at San Antonio, One UTSA Circle, San Antonio, TX 78249, USA
[11] Max-Planck-Institut für Radioastronomie, Auf dem Hügel 69, D-53121 Bonn, Germany
[12] Department of Space, Earth and Environment, Chalmers University of Technology, Onsala Space Observatory, SE-439 92 Onsala, Sweden
[13] Shanghai Astronomical Observatory, Chinese Academy of Sciences, 80 Nandan Road, Shanghai 200030, People's Republic of China
[14] Key Laboratory of Radio Astronomy, Chinese Academy of Sciences, Nanjing 210008, People's Republic of China
[15] Department of Astronomy, University of Illinois at Urbana-Champaign, 1002 West Green Street, Urbana, IL 61801, USA
[16] Massachusetts Institute of Technology Haystack Observatory, 99 Millstone Road, Westford, MA 01886, USA
[17] Institut für Theoretische Physik, Goethe-Universität Frankfurt, Max-von-Laue-Straße 1, D-60438 Frankfurt am Main, Germany
[18] Tsung-Dao Lee Institute and School of Physics and Astronomy, Shanghai Jiao Tong University, Shanghai, 200240, People's Republic of China
[19] Mizusawa VLBI Observatory, National Astronomical Observatory of Japan, 2-12 Hoshigaoka, Mizusawa, Oshu, Iwate 023-0861, Japan
[20] Department of Astronomical Science, The Graduate University for Advanced Studies (SOKENDAI), 2-21-1 Osawa, Mitaka, Tokyo 181-8588, Japan
[21] Las Cumbres Observatory, 6740 Cortona Drive, Suite 102, Goleta, CA 93117-5575, USA
[22] Department of Physics, University of California, Santa Barbara, CA 93106-9530, USA
[23] Institut für Theoretische Physik und Astrophysik, Universität Würzburg, Emil-Fischer-Str. 31, D-97074 Würzburg, Germany
[24] Department of History of Science, Harvard University, Cambridge, MA 02138, USA
[25] Department of Physics, Harvard University, Cambridge, MA 02138, USA
[26] Department of Astronomy, School of Physics, Peking University, Beijing 100871, People's Republic of China
[27] Kavli Institute for Astronomy and Astrophysics, Peking University, Beijing 100871, People's Republic of China
[28] ASTRAVEO, LLC, PO Box 1668, Gloucester, MA 01931, USA
[29] Department of Astrophysics, Institute for Mathematics, Astrophysics and Particle Physics (IMAPP), Radboud University, P.O. Box 9010, 6500 GL Nijmegen, The Netherlands
[30] Institut de Radioastronomie Millimétrique, 300 rue de la Piscine, F-38406 Saint Martin d'Hères, France
[31] Korea Astronomy and Space Science Institute, Daedeok-daero 776, Yuseong-gu, Daejeon 34055, Republic of Korea
[32] University of Science and Technology, Gajeong-ro 217, Yuseong-gu, Daejeon 34113, Republic of Korea
[33] Department of Space, Earth and Environment, Chalmers University of Technology, Onsala Space Observatory, SE-43992 Onsala, Sweden
[34] Departament d'Astronomia i Astrofísica, Universitat de València, C. Dr. Moliner 50, E-46100 Burjassot, València, Spain
[35] Observatori Astronòmic, Universitat de València, C. Catedrático José Beltrán 2, E-46980 Paterna, València, Spain
[36] School of Physics & Astronomy, Shanghai Jiao-Tong University, 800 Dongchuan Road, Shanghai, 200240, People's Republic of China
[37] Villanova University, Mendel Science Center Rm. 263B, 800 E Lancaster Avenue, Villanova PA 19085, USA
[38] Frankfurt Institute for Advanced Studies, Ruth-Moufang-Strasse 1, D-60438 Frankfurt, Germany
[39] School of Mathematics, Trinity College, Dublin 2, Ireland
[40] Department of Astrophysical Sciences, Peyton Hall, Princeton University, Princeton, NJ 08544, USA
[41] Center for Computational Astrophysics, Flatiron Institute, 162 Fifth Avenue, New York, NY 10010, USA
[42] Frontier Research Institute for Interdisciplinary Sciences, Tohoku University, Sendai 980-8578, Japan
[43] Astronomical Institute, Tohoku University, Sendai 980-8578, Japan
[44] Instituto de Radioastronomía Milimétrica, IRAM, Avenida Divina Pastora 7, Local 20, E-18012, Granada, Spain
[45] Key Laboratory for Research in Galaxies and Cosmology, Chinese Academy of Sciences, Shanghai 200030, People's Republic of China

[46] School of Astronomy and Space Sciences, University of Chinese Academy of Sciences, No. 19A Yuquan Road, Beijing 100049, People's Republic of China
[47] Bard College, 30 Campus Road, Annandale-on-Hudson, NY 12504, USA

Abstract

We report measurements of the gravitationally lensed secondary image—the first in an infinite series of so-called "photon rings"—around the supermassive black hole M87[*] via simultaneous modeling and imaging of the 2017 Event Horizon Telescope (EHT) observations. The inferred ring size remains constant across the seven days of the 2017 EHT observing campaign and is consistent with theoretical expectations, providing clear evidence that such measurements probe spacetime and a striking confirmation of the models underlying the first set of EHT results. The residual diffuse emission evolves on timescales comparable to one week. We are able to detect with high significance a southwestern extension consistent with that expected from the base of a jet that is rapidly rotating in the clockwise direction. This result adds further support to the identification of the jet in M87[*] with a black hole spin-driven outflow, launched via the Blandford–Znajek process. We present three revised estimates for the mass of M87[*] based on identifying the modeled thin ring component with the bright ringlike features seen in simulated images, one of which is only weakly sensitive to the astrophysics of the emission region. All three estimates agree with each other and previously reported values. Our strongest mass constraint combines information from both the ring and the diffuse emission region, which together imply a mass-to-distance ratio of $4.20^{+0.12}_{-0.06}\,\mu$as and a corresponding black hole mass of $(7.13 \pm 0.39) \times 10^9\,M_\odot$, where the error on the latter is now dominated by the systematic uncertainty arising from the uncertain distance to M87[*].

Unified Astronomy Thesaurus concepts: Black hole physics (159); Astronomy data modeling (1859); Computational astronomy (293); Submillimeter astronomy (1647); Very long baseline interferometry (1769); General relativity (641)

1. Introduction

Radio emission from the immediate vicinity of the supermassive black hole M87[*] was used to reconstruct the first-ever image of a black hole, estimate its mass, and interpret its theoretical environment by the Event Horizon Telescope (EHT) Collaboration (Event Horizon Telescope Collaboration et al. 2019a, 2019b, 2019c, 2019d, 2019e, 2019f, hereafter Papers I-VI).

The analyses behind these findings included multiple image-reconstruction algorithms, model fitting in the visibility domain employing various geometric shapes, and an extensive investigation of physical emission models. The latter are based on a large library of simulations that model the source as a hot, magnetized accretion flow, that form the input for theoretical model images constructed via ray-tracing and solving the equations of radiative transfer for a thermal population of relativistic electrons emitting synchrotron radiation. Typically, these models predict images with both a sharp ring component —i.e., associated with the location of photon rings in the underlying spacetime—as well as a comparatively diffuse but still compact emission structure (see, e.g., Paper V).

Image reconstructions, model fitting to geometric shapes, and direct fitting to general relativistic magnetohydrodynamical (GRMHD) synchrotron models all yielded an inferred mass for M87[*] of $(6.5 \pm 0.7) \times 10^9\,M_\odot$, which agrees with stellar-dynamical mass inferences of $(6.14^{+1.07}_{-0.62}) \times 10^9 M_\odot$ (Gebhardt et al. 2011; Paper VI). The error in each method was estimated based on the variable emission structure from the GRMHD-based model images.

In the meantime, novel imaging schemes have been developed that can either approximate (Arras et al. 2019; Sun & Bouman 2020) or directly sample (Broderick et al. 2020b;

Pesce 2021) the posterior distribution over possible image structures. The Bayesian nature of these schemes yield meaningful posterior distributions for the images. These posteriors permit a more rigorous characterization of the credibility of image features and a measure of image consistency. In addition, they permit a hybrid approach that combines image reconstruction with modeling specific expected features. This is demonstrated in Broderick et al. (2020b), where imaging is accomplished with a "nonparametric" model comprised of a rectilinear raster of control points, and additional geometric components (Gaussians, rings, etc.). Of particular interest here is the ability to reconstruct ring features in the data beyond the diffraction limit, provided the signal-to-noise ratios (S/Ns) of the measured complex visibilities are sufficiently high.

Such ring features are theoretically expected outcomes in black hole images due to the propagation of photons in close proximity to the black hole, and the associated strong gravitational lensing predicted by general relativity. It is useful to think of the resulting image that is measured at infinity to be composed of a *direct* emission component that is dominated by the typically nontrivial and uncertain astrophysical environment, plus a series of *ring* components that are confined to distinct narrow regions (far less influenced by the details of the overall flow structure), which arise from photons that traversed the black hole once, twice, and so on before reaching a distant observer (Bardeen 1973; Broderick et al. 2022). Thus far, the M87[*] images present the total image structure, i.e., the sum of all of those components; the diffraction-limited image reconstructions in Paper IV cannot distinguish the ring components from the rest of the emission directly.

In all of the theoretical models presented in Paper V that were consistent with the data, the direct emission provided the majority of the flux, with a substantial minority arising from the first higher-order image component; in what follows we will refer to these as the $n = 0$ and $n = 1$ "photon rings," respectively, despite the former often not forming a ring. Based on inspection of the GRMHD library presented in Paper V, the $n = 1$ ring typically contains 10%–30% of the total compact flux, depending on the

model (e.g., Gralla et al. 2019; Johnson et al. 2020). Here, we demonstrate that statistically preferred reconstructions are achieved when a thin ring is included in addition to the standard nonparameteric image-reconstruction component. The thin ring is then identified with the $n = 1$ photon ring of the underlying spacetime. Interpreting the separate emission components as the $n = 1$ and $n = 0$ photon rings provides a powerful mapping of spacetime that is far less sensitive to the astrophysical processes in the emitting region than previous analyses (Broderick et al. 2022).

In this paper we report the results of applying the hybrid image model from Broderick et al. (2020b) to the M87* 2017 EHT data set. By fitting a geometric ring model component simultaneously with a flexible image component, we are able to isolate the $n = 1$ photon ring from the surrounding diffuse emission. We demonstrate that our reconstructed emission structure is in agreement with prior EHT imaging results, and the properties of the $n = 1$ ring yield novel constraints on the black hole mass with significantly reduced systematic uncertainties. Furthermore, because the bright ring emission is effectively extracted by the geometric model component, the image component is free to capture subtler details within the remaining diffuse emission than would otherwise be possible. We find that the removal of the bright foreground ring uncovers additional low-brightness image structures that are consistent with originating from the base of the forward jet; the observed brightness asymmetry in context with previous EHT results constraining the black hole spin orientation Paper V aligns with expectations for a jet driven by the Blandford–Znajek mechanism (Blandford & Znajek 1977).

The structure of the paper is as follows. In Section 2 we summarize the algorithm used to reconstruct the images. We present the reconstructed, structure-agnostic images in Section 3, before presenting the hybrid reconstructions in Section 4. In Section 5 we describe how our findings are related to the black hole parameters. The implications of the structure and evolution of the diffuse emission within the broader context of M87* are collected in Section 6. We summarize and conclude in Section 7.

2. Imaging Algorithm Summary

We employ the forward-modeling Markov Chain Monte Carlo (MCMC) algorithm presented in Broderick et al. (2020b) and implemented in the THEMIS analysis framework (Broderick et al. 2020a). In this scheme, the image is forward-modeled by a rectilinear grid of control points, at which the intensity is a free parameter, and between which the intensity is modeled via an approximate cubic spline. Station gains are simultaneously modeled, and are assumed to be fixed in time over a single scan. For the current work, this algorithm has been supplemented in four ways.

First, we have included the field of view (FOV) as two additional parameters in the underlying image models (one for each dimension in the image plane). This change promotes the two FOVs from hyperparameters that must be manually surveyed to parameters that are continuously explored in a fashion more consistent with the general Bayesian approach employed. It also permits efficient exploration of asymmetric FOVs, i.e., different FOVs in the two directions of the rectilinear grid. While this flexibility makes only a small difference for the results presented here, it does enable analysis of highly asymmetric and extended systems (e.g., active galactic nuclei jets).

Second, we permit a rotation of the rectilinear grid. This change permits the control points to optimally arrange themselves within the confines of the grid. Typically, this freedom permits smaller grid dimensions than grids that are fixed to be oriented along the cardinal directions. Again, this additional flexibility makes only a modest difference in the applications here.

Third, we make use of an updated set of samplers implemented within THEMIS. Details on the sampler, including demonstrations, may be found in Tiede (2021). In summary, the improved sampler makes use of a deterministic even–odd swap tempering scheme (Syed et al. 2019) using the Hamiltonian Monte Carlo sampling kernel from the Stan package (Carpenter et al. 2017). MCMC chain convergence is assessed using standard criteria, including integrated autocorrelation time, approximate split $\hat{R}$, and visual inspection of individual traces.

Fourth, we fit to complex visibilities rather than some combination of visibility or closure amplitudes and phases. This requires that we reconstruct the time-variable station gain phases in addition to their amplitudes. Both are stable across a 10 minute scan. Fitting the complex visibilities simplifies the treatment of the errors at low S/N: thermal errors are strictly Gaussian (Thompson et al. 2017). It also improves the structure of the likelihood surface to be explored, which is both smoother and has fewer modes in this case.

Fit quality is assessed using the χ^2 statistic, comparing log-likelihoods, and by inspecting the distribution of residuals.

3. Image Reconstructions

Prior to applying the complete hybrid imaging model, we first perform nonhybrid image reconstructions to more easily enable comparison with previous imaging work and to provide context for subsequent interpretation of the hybrid images.

We reconstruct images for each of the four EHT observations of M87* taken in 2017 April. The observations were carried out using two frequency bands (Paper III), which we refer to as a high band and a low band, and we image both bands simultaneously. We assume that the image structure is shared across bands, such that a single image is produced for each day, but we permit the station gains to be completely independent among bands. Prior to fitting, we preprocess the visibility data as described in Broderick et al. (2020b): we coherently time-average the complex visibilities within each scan, and we add a systematic uncertainty of 1% in quadrature to the thermal uncertainties to account for residual calibration errors. This additional error budget is motivated by the analysis of nonclosing errors in Paper III and the same as that found in Papers V and VI sufficient to produce high-quality fits. The model we employ uses a 5×5 grid of control points to capture the image structure, and a large-scale asymmetric Gaussian (a major-axis FWHM above 0.2 mas; see Appendix A for details) to accommodate structure seen on only the shortest baselines (again utilizing the hybrid modeling+imaging approach).

Table 1 provides an accounting of the parameters and data quantities used for each of the fits, and it lists various fit statistics for each of our reconstructions. The quantities most comparable to the fit statistics reported in Table 5 of Paper IV and Table 2 of Paper VI would be the $\chi^2/(N_{\mathrm{data,HI}} + N_{\mathrm{data,LO}})$, which here range from 0.58 to 0.93 and are otherwise comparable to those reported previously. Direct comparisons with the complex visibility data and the corresponding residuals are shown for representative days in Figure 1.

Figure 2 shows the resulting image reconstructions for each of the four days. The top row shows the maximum-likelihood samples from each chain, the middle row shows the posterior means, and the bottom row shows the posterior standard deviations. We find

Table 1
Fit Quality Assessment

Day	Model[a]	N_{params}	$N_{\mathrm{data,\,HI}}$[b]	$N_{\mathrm{data,\,LO}}$[b]	$N_{\mathrm{g,HI}}$[b]	$N_{\mathrm{g,LO}}$[b]	χ^2_{HI}	χ^2_{LO}	χ^2[c]	$\Delta\mathrm{BIC}$[d]	$\Delta\mathrm{AIC}$[e]
April 5	$\mathrm{I}_{5\times5}$+A	34	336	336	162	162	295.2	246.4	628.0	⋯	⋯
	$\mathrm{I}_{5\times5}$+A+X	41	336	336	162	162	219.6	196.2	454.7	−127.7	-107.4
April 6	$\mathrm{I}_{5\times5}$+A	34	548	568	226	243	436.3	376.2	872.1	⋯	⋯
	$\mathrm{I}_{5\times5}$+A+X	41	548	568	226	243	356.8	344.0	756.2	−66.8	-68.9
April 10	$\mathrm{I}_{5\times5}$+A	34	182	192	79	73	87.9	96.7	216.5	⋯	⋯
	$\mathrm{I}_{5\times5}$+A+X	41	182	192	79	73	80.5	93.2	194.0	18.9	35.5
April 11	$\mathrm{I}_{5\times5}$+A	34	432	446	185	190	388.9	338.1	800.6	⋯	⋯
	$\mathrm{I}_{5\times5}$+A+X	41	432	446	185	190	365.6	313.6	742.6	−10.5	-8.0

Notes.
[a] Model components are as follows: an $N \times M$ dimensional image raster ($\mathrm{I}_{N\times M}$), a large-scale asymmetric Gaussian (A), and a slashed ring (X). Detailed descriptions of the model components and priors can be found in the main text and Appendix A.
[b] Each complex visibility is counted as two data points ($N_{\mathrm{data,HI/LO}}$). Similarly, each complex gain is counted as two gain parameters ($N_{\mathrm{g,HI/LO}}$).
[c] Includes contributions from the gain priors.
[d] Differences between the Bayesian information criterion (BIC) with and without the slashed ring. The BIC is defined by $\chi^2 + k \ln(N)$, where $k \equiv N_{\mathrm{params}} + N_{\mathrm{g,HI}} + N_{\mathrm{g,LO}}$ is the total number of model parameters and $N \equiv N_{\mathrm{data,HI}} + N_{\mathrm{data,LO}}$.
[e] Differences between the Akaike information criterion (AIC) with and without the slashed ring. The AIC is defined by $\chi^2 + 2k + 2k(k+1)/(N-k-1)$, where k and N are defined as they are for the BIC.

that the posterior mean images show a qualitatively similar ringlike structure to image reconstructions produced using regularized maximum-likelihood methods in Paper IV, though we note that we have not imposed any comparable regularization (e.g., maximum entropy, total variation) on our likelihood function. The general shape, size, and total flux of the emission structure are similar across all four days, as is the pronounced north–south asymmetry in the brightness distribution. We find that the image control point raster prefers a FOV of ∼50 μas in both axis directions and a modest rotation with respect to the equatorial coordinate system (see Appendix A).

The bottom row of Figure 2 illustrates a measure of the uncertainty in the image reconstructions, as previously demonstrated in Broderick et al. (2020b). We find that the uncertainty is not uniform across the image, nor does it seem to be proportional to the image intensity. Rather, the uncertainty tends to be lowest within an approximately circular region running azimuthally around the ring, and it increases both radially inwards and outwards of this region. We note that this behavior contrasts with the appearance of the image uncertainty reported in Sun & Bouman (2020); we do not explore these differences in this paper, but we expect that they arise primarily from the large differences in likelihood and prior specification between these two algorithms.

4. Ring Reconstructions

The image model described in the previous section is incapable of reconstructing features on scales much smaller than the raster spacing, which is comparable to the nominal array resolution of ∼20 μas. However, the lowest-order lensed image around the black hole—i.e., the $n = 1$ photon ring—is expected to have a thickness of only ∼1 μas (Johnson et al. 2020). While we may not expect to be able to spatially resolve the thickness of this ring with the 2017 EHT array, its ∼40 μas diameter should still imprint itself on the visibility data. By enforcing the prior expectation that a putative $n = 1$ component of the observed emission structure should originate from a thin ring (i.e., one having a thickness that is much less than its diameter), Broderick et al. (2020b) showed that the diameter of the photon ring could be reliably recovered from EHT-like synthetic data sets generated from input images produced from GRMHD simulations.

Following Broderick et al. (2020b), we perform hybrid imaging of the four M87* data sets, in which we fit for a "slashed ring" model component alongside the image and large-scale Gaussian described in the previous section. For the M87* black hole, which has a spin-axis inclination of ≲20° with respect to the line of sight (Walker et al. 2018; Paper V), the photon ring is expected to have a nearly circular geometry with only small (≲2%; Johnson et al. 2020) deviations from circularity even for large spin values. We thus model the ring as a thin (fractional thickness less than 5%; see Appendix A) circular annulus with a linear brightness gradient ("slash"), and we permit the diameter, flux, and slash magnitude and orientation to be free parameters. The thickness parameter is restricted by a tight prior that forces it to be <5% of the diameter. Additionally, we permit the center coordinates of the ring model component to drift with respect to the center of the image model component. We describe the model and prior distribution specification in more detail in Appendix A. Direct comparisons with the complex visibility data and the corresponding fit residuals for representative days are presented in Figure 3, and indicate high-quality fits across the entirety of the range of baselines probed by the EHT.

As tabulated in Table 1, we find lower χ^2 values when fitting a hybrid image to the data relative to fitting the image model described in Section 3. For comparison with Table 5 of Paper IV and Table 2 of Paper VI, the analogous χ^2 quantities to those reported there range from 0.52 to 0.86, again a roughly comparable fit quality. Such improved fit quality is expected given the increased complexity of the hybrid image model, but information criteria considerations indicate that the fit improvement outweighs the additional model complexity for all but the April 10 data set. The April 10 data set is the sparsest of the four, containing a factor of ∼2–3 fewer data points than any of the other data sets, and the information criteria indicate that the increased complexity of the hybrid images is not statistically necessary in this case.[49] However, we note that the statistical preference for a ring component in the other three data sets—

---

[49] Note that this does not preclude the possibility of more complex structure, as is preferred on other days. Rather, this only indicates that more complex structures are not required to explain the data on April 10.
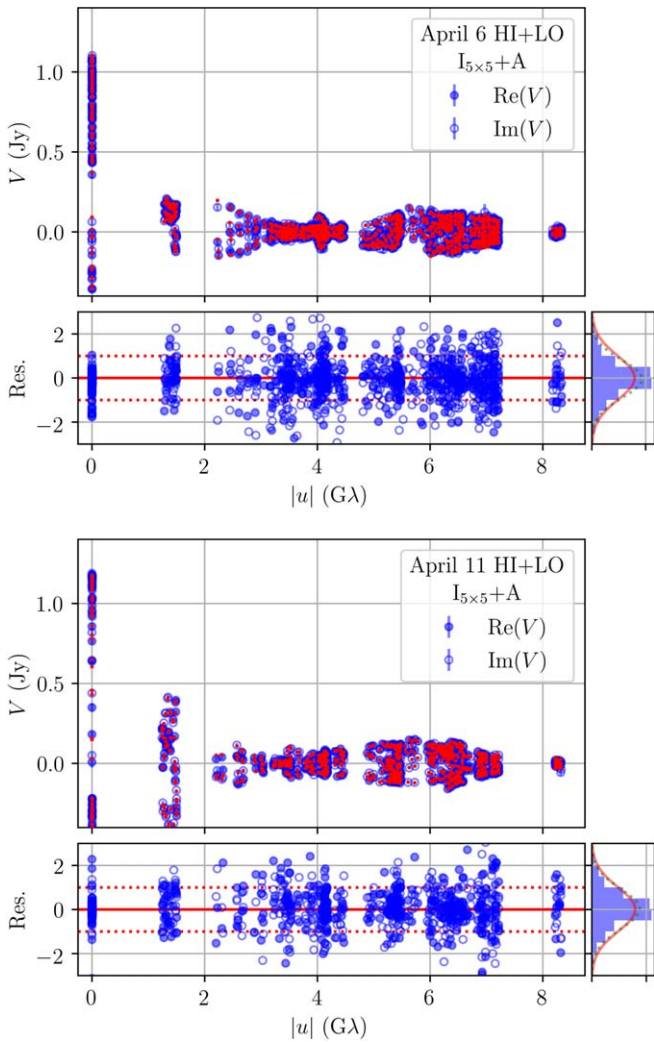
Figure 1. Direct comparisons between the model and measured values of the complex visibilities for two representative days for the combined high- and low-band data. In each plot, the upper panel shows the maximum-likelihoood $I_{5\times5}+A$ model predictions (red dots) for real (filled) and imaginary (open) components of the complex visibilities (blue points). Normalized residuals are shown in the bottom panel with $\pm1\sigma$ indicated for reference (red dotted lines). To the right of the residuals, the distributions of normalized residuals (blue histograms) are shown on the right in comparison to a unit-variance normal distribution (red) and the Gaussian with the same mean and variance as the residuals (green dotted).

for which the coverage is more complete and the emission structure correspondingly better constrained—implies its presence in the April 10 data set, as well.

Our hybrid image reconstructions for each of the four days are shown in Figure 4. We find that after convolution with a 15 μas Gaussian beam, the gross structural properties of the emission qualitatively match those recovered from the imaging in Section 3 (see Figure 2) and image reconstructions in Paper IV, though with an evident preference for a smoother and more uniformly circular emission structure in the hybrid images. The ability of the thin ring model component to capture aspects of the source structure frees the remaining image model component to devote its flexibility to recovering fainter features. This increased focus on fainter structures can also be seen in the behavior of the image control point raster, which shows a broader east–west extent for the hybrid image fits than for the image-only fits (see Appendix A).

Figure 5 shows the hybrid image reconstructions with the ring and image components separated. The slashed ring model component is shown at nearly its native resolution; it is smoothed by 0.5 μas for visualization purposes only. The diffuse emission map is displayed without any additional convolution (in contrast to Figures 4 and 2). In this figure, the slashed ring model component is visually distinct from the much-lower-brightness diffuse emission associated with the image model component.

Though the model permits both the ring and image components to drift freely with respect to one another, we find that the data prefer reconstructions in which the two components are nearly concentric. We see that the diffuse emission is primarily concentrated along the southern portion of the ring, helping to define several "knots" of emission; a by-eye decomposition indicates that there are approximately two such knots on April 5 and 6, with a third knot appearing at the southernmost point of the ring on April 10 and 11. Additionally, we find that all four days show a feature that is significantly detected to the southwest of the ring. This southwestern component is present in some of the reconstructions from Paper IV and features more prominently in Arras et al. (2022) and Carilli & Thyagarajan (2022), but only the latter two works provided any comment; we discuss the potential origin of and implications for this feature in Section 6.2.

The reconstructed flux densities in both the image and ring model components are listed in Table 2, and we find that the ring component contains between ~54%–64% of the total flux in the image. This range exceeds the fraction of flux contained in the narrow ringlike features in GRMHD simulations, from which we anticipate only ~10%–30% of the total image flux to be contained in the narrow ring. The measured fluxes are, however, consistent with the results from Broderick et al. (2020b) for hybrid image reconstructions of simulated data. The excess ring flux appears to be a consequence of the absorption of a portion of the surrounding direct emission into the ring component. By virtue of their sparse (u,v) coverage and finite S/N, the EHT observations have an effective angular resolution limit of approximately ~10 μas (Paper IV), which is smaller than the nominal beam size of ~20 μas but still much larger than the anticipated $n=1$ ring thickness of ~1–2 μas. Image structures on scales smaller than this ~10 μas threshold are effectively unresolved by the array. Our hybrid image model priors confine the ring thickness to be $\lesssim$5% of the ring radius (roughly 1 μas; see Appendix A), but source flux contained within an annulus of thickness ~10 μas around the ring radius is structurally indistinguishable from flux residing within the ring itself. In GRMHD simulations, such an annulus contains roughly ~50%–80% of the total source flux, consistent with the results in Table 2. Broderick et al. (2020b) have demonstrated that this excess flux capture does not appear to substantially bias the recovered $n=1$ ring radius.

Figure 6 shows the posterior distributions for the ring component radius parameter on all four days. The radius measurements are consistent with being constant across the week; the apparent evolution from April 6 to April 11 is a modest 2σ tension after inclusion of the appropriate trials factor. Combining the ring radius measurement across all days yields $\theta_{\mathrm{ring}} = 21.74 \pm 0.10 \mu$as. Posteriors for other ring properties (flux, position angle, thickness) can be found in Appendix B, and are similarly consistent among days. The
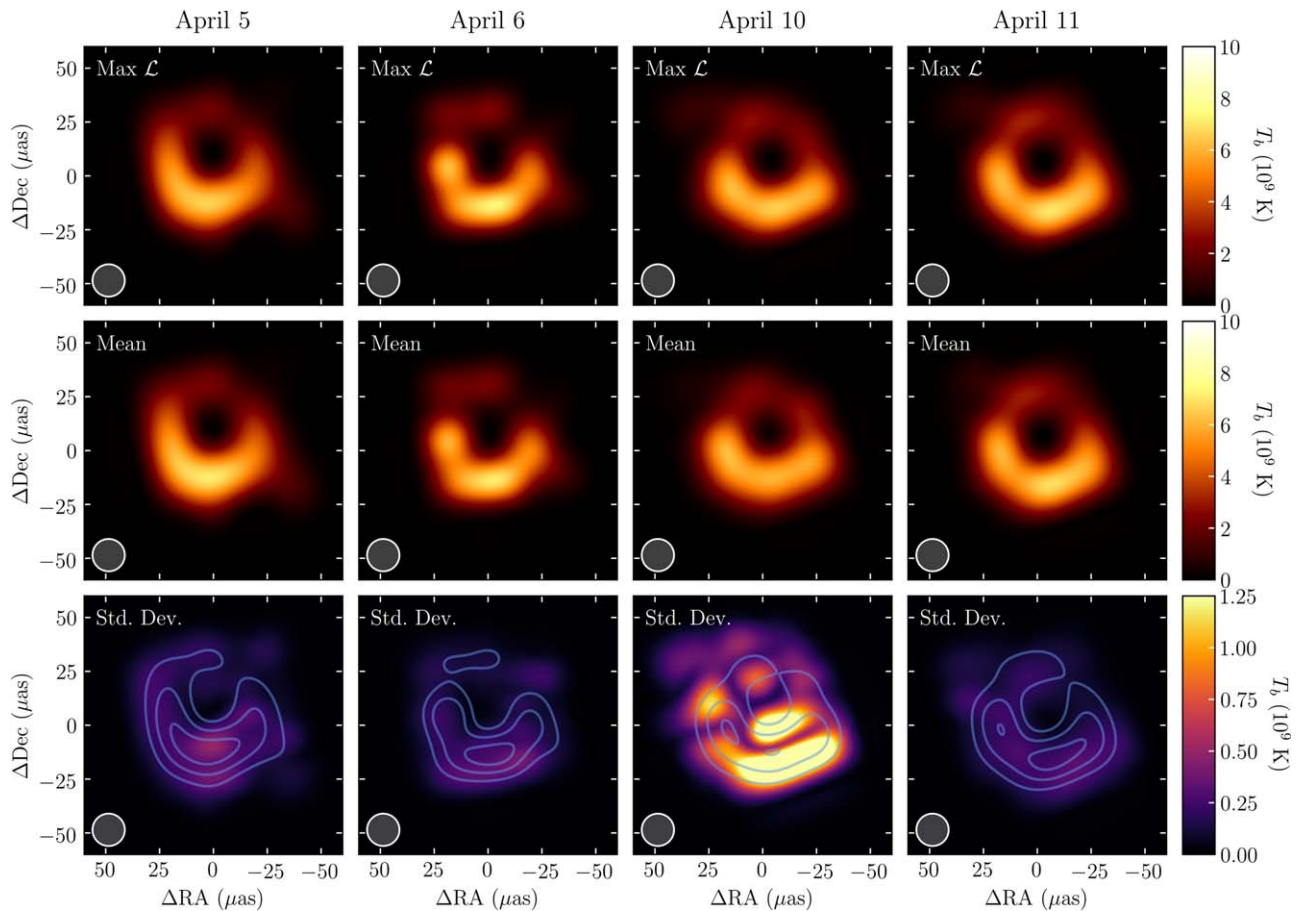
Figure 2. Brightness temperature maps of M87 based on the raster image model. Shown are the maximum-likelihood sample (top), average image (middle), and standard deviation with contours from the average image overlaid ranging from 2×10^9 K to 8×10^9 K in steps of 2×10^9 K (bottom). Each map has been smoothed by a 15 μas Gaussian beam, shown in the lower left of each panel, resulting in a combined effective resolution of approximately 20 μas to make these more directly comparable with the results in Paper IV.

radius of the direct emission region, θ_{diff}, is measured from the ring center by computing the radial location of the brightness peak in the image component. Though we note that the direct emission does not necessarily form a closed ring on any day, this definition nevertheless presents the most consistent measure of direct emission ring size to that invoked in Broderick et al. (2022). We find that the direct emission radius is a factor of ~10 more uncertain than that of the ring component; we generate posteriors for θ_{diff} on each day from the hybrid image reconstructions, and the resulting values are listed in Table 2.

5. Physical Parameters of the Black Hole

Most directly constrained, and most comparable to other measurements of the mass, is the angular scale $\theta_M \equiv GM/c^2 D$, where D is the distance to M87*. This is related to the angular radius of the bright ring. However, it is subject to additional systematic uncertainties associated with the nature of this relationship, dominated by a systematic bias associated with the location of the emission region and the dependence on black hole spin.

Here we consider three methods for estimating θ_M and the corresponding mass, $M = M_9 \times 10^9 \, M_\odot$. All of these identify the bright ringlike structure in the image with the $n = 1$ photon ring, produced by photons that execute a half-orbit about the

black hole prior to reaching the distant image plane. This is motivated both geometrically—higher-order photon rings are suppressed exponentially (Johnson et al. 2020)—and from astrophysical predictions ranging from semi-analytical modeling (Broderick et al. 2016) to GRMHD simulations (Paper V; Gammie et al. 2003; Abramowicz 2013; Porth et al. 2019). They differ in the manner in which they attempt to systematically address the dependence on spin and the relationship to the asymptotic ($n = \infty$) photon ring, which defines the edge of the black hole shadow.

In all cases, where we transform from an angular measurement of the mass, θ_M, to a physical measurement, we will assume a distance of $D = 16.8 \pm 0.8$ Mpc (see Appendix I of Paper VI, and references therein). These measurements and relevant comparisons are collected in Table 3.

5.1. Direct Mass Estimates

As described in Broderick et al. (2022), the sensitivity of the size of the $n = 1$ photon ring to the location of an equatorial emission region is bounded. This is in contrast to the $n = 0$ photon ring, which can grow arbitrarily large with more distant equatorial emission. As a result, with the detection of the $n = 1$ photon ring, it is now possible to place a limit on the mass that is weakly dependent on the physics of the emission region, subject to the assumption that this emission is confined to near-
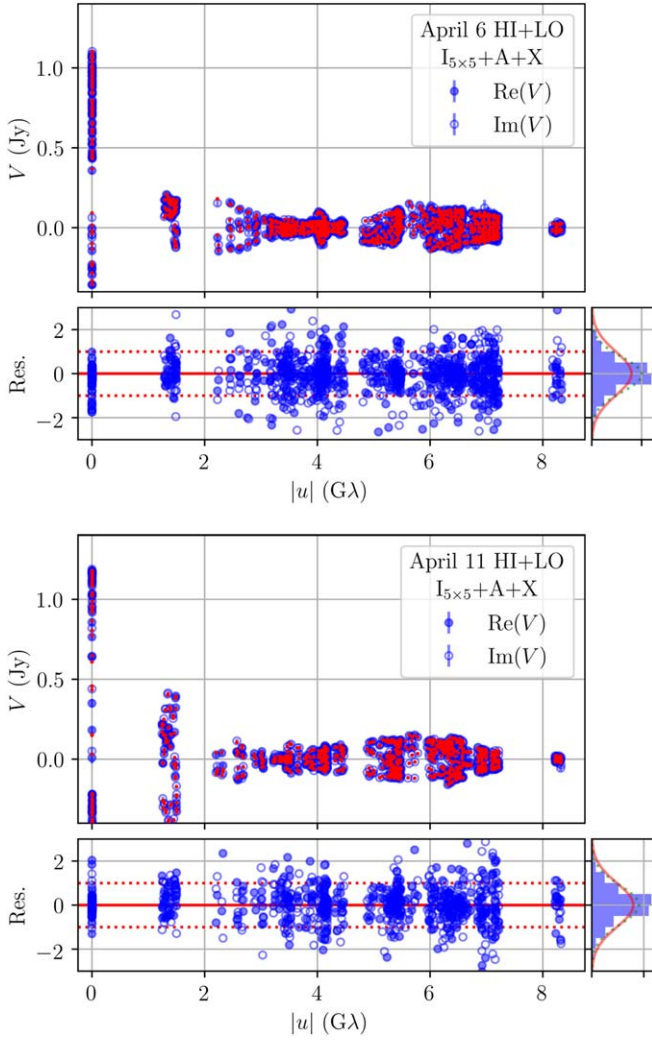
Figure 3. Similar to Figure 1 for the $I_{5\times5}$+A+X model.

equatorial regions, e.g., as anticipated by Magnetically Arrested Disk (MAD) models.[50]

The size of the $n = 1$ photon ring from equatorial emission is given by

$$\theta_{n=1} = \vartheta_{n=1}(a, r_{em}, i)\, \theta_M, \qquad (1)$$

where $\vartheta_{n=1}(a, r_{em}, i)$ is a dimensionless function that ranges from 4.30 and 6.17 for polar observers, depending on the black hole spin, a, and radius of the emission peak, r_{em}. Therefore, from the measurement of $\theta_{n=1}$ it is possible to generate an *astrophysics-independent* limit on the mass of M87*:

$$\begin{aligned} \theta_M &= \vartheta_{n=1}^{-1}\, \theta \\ &= 4.15 \pm 0.02 \pm 0.74|_{\vartheta_{n=1}}\ \mu\text{as}, \end{aligned} \qquad (2)$$

where we have separately indicated statistical uncertainty and the systematic uncertainty in the relationship between the $n = 1$ ring and the mass. The corresponding mass estimate is

$$M_9 = 7.06 \pm 0.03 \pm 1.26|_{\vartheta_{n=1}} \pm 0.34|_D, \qquad (3)$$

---

[50] This condition may be violated by distant emission along the line of sight behind the black hole. In such a case, however, it would be difficult to understand why the interior of the shadow does not exhibit a bright feature from a presumably foreground partner region.

where the systematic uncertainty associated with that on the distance is also separately stated.

5.2. Corrected Mass Estimates

The $n = 1$ photon ring is biased relative to the asymptotic (i.e., $n = \infty$) photon ring associated with the boundary of the black hole shadow. The degree to which it is biased depends on the spatial distribution of the emission region (Broderick et al. 2020b, 2022). In Appendix C we describe two attempts to estimate the degree of this bias. The first, described in detail in Appendix C.1, is based solely on geometric arguments, assumes a polar observer, and is subject to the size constraints reported in Paper VI. These are shown in Figure 7. These indicate that this bias is robustly limited to less than 1.3 μas, and typically significantly smaller.

A potentially more relevant estimate based on GRMHD simulations is described in Figure 8. We make use of the GRMHD simulations reported in Paper V.

These incorporate two important additional effects: the small but nonzero inclination (i ranges from $12°$ to $22°$) and emission from above and below the equatorial plane. Both of these tend to shrink the size of the $n = 1$ photon ring, as seen in Figure 8.

Models that exhibit extended emission, e.g., the $R_{high} = 1$ simulations, can have biases that exceed 1 μas. However, these are excluded by the M87* size constraints Paper V. When only models that are consistent with the source size and ancillary limits described in Paper V are considered, the size of the bias is below 0.8 μas; the typical shift is $\Delta\theta_{n=\infty} = 0.56 \pm 0.32$ μas.

Like that of the $n = 1$ photon ring, the angular size of the asymptotic photon ring is given by

$$\theta_{n=\infty} = \vartheta_{n=\infty}(a, i)\theta_M, \qquad (4)$$

where $\vartheta(a, i)$ is another dimensionless function, ranging from 4.90 to 5.20 depending on spin for the inclinations relevant for M87*. This range is considerably smaller than that for $\vartheta_{n=1}$, corresponding to a significantly reduced dependence on the details of the emission region, which is otherwise encoded in $\Delta\theta$. Thus, the uncertain spin introduces only an additional 3% systematic uncertainty in the relationship between the asymptotic photon ring radius and the mass.

Therefore, the mass of M87* in angular units is given by

$$\begin{aligned} \theta_M &= \vartheta_{n=\infty}(a, i)^{-1}(\theta_{n=1} - \Delta\theta_{n=\infty}) \\ &= 4.22 \pm 0.02 \pm 0.06|_{\Delta\theta} \pm 0.16|_\vartheta\ \mu\text{as}, \end{aligned} \qquad (5)$$

where again we have separately listed the random measurement error and the systematic errors associated with the emission region ($\Delta\theta$) and spin (ϑ). This corresponds to a mass estimate of

$$M_9 = 7.18 \pm 0.04 \pm 0.11|_{\Delta\theta} \pm 0.27|_\vartheta \pm 0.34|_D, \qquad (6)$$

5.3. Joint Mass/Spin Estimate

Finally, following Broderick et al. (2022), we attempt to jointly reconstruct the size of the $n = 0$ and $n = 1$ photon rings, as listed in Table 2. This leverages the additional information presented by the diffuse emission to constrain the location of the emission region. However, because there is limited evolution in the maps during the 2017 EHT observing campaign and the simulated analyses in Broderick et al. (2022), the constraint on spin will be weak, rendering this primarily a demonstration in principle.
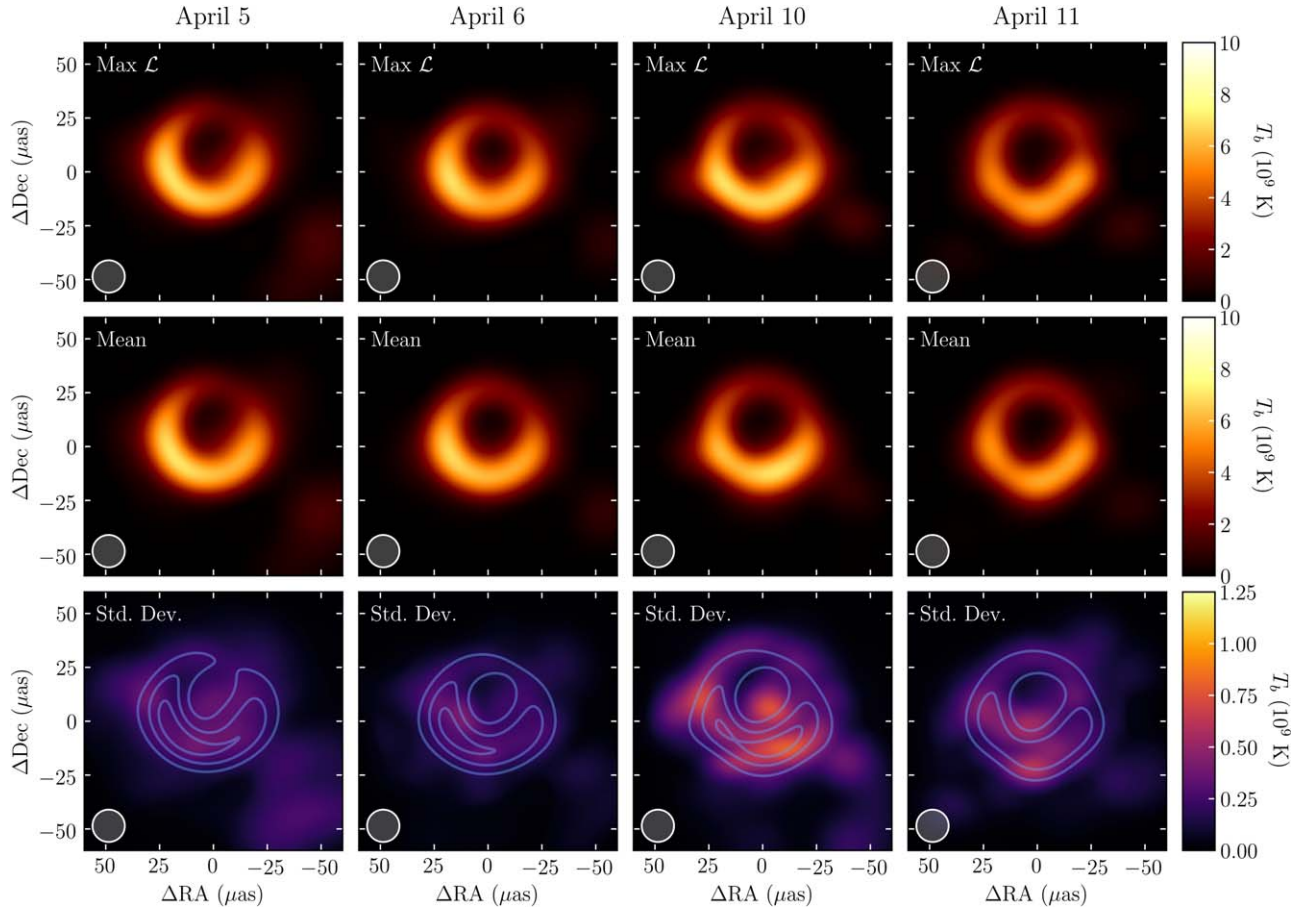
Figure 4. Brightness temperature maps of M87 based on the hybrid ring+image model. Shown are the maximum-likelihood sample (top), average image (middle), and standard deviation with contours from the average image overlaid ranging from 2×10^9 K to 8×10^9 K in steps of 2×10^9 K (bottom). Each map has been smoothed by a 15 μas Gaussian beam, shown in the lower left of each panel, resulting in a combined effective resolution of approximately 20 μas to make these more directly comparable with the results in Paper IV.

Details for the model, likelihood, and method of sampling are collected in Appendix D. The resulting joint posterior on θ_M and a is shown in Figure 9. Marginalizing over spin, we find for the mass

$$\theta_M = 4.20^{+0.12+0.23}_{-0.06-0.10} \ \mu\text{as}, \qquad (7)$$

and

$$M_9 \ = \ 7.13^{+0.20+0.39}_{-0.11-0.17} \pm 0.34|_D, \qquad (8)$$

where the indicated errors correspond to 1σ and 2σ. Note that because the spin is simultaneously reconstructed, these include what has previously been identified as the systematic uncertainties associated with the $n = 1$ photon ring size bias and spin.

After marginalizing over mass, the spin estimate is

$$a \ = \ 1.0^{+0+0}_{-0.5-1}, \qquad (9)$$

where again the indicated errors correspond to 1σ and 2σ. As anticipated, the spin is effectively unconstrained, although there appears to be a very weak preference for high spin.

To demonstrate this we repeated the analysis with synthetic size measurements constructed from the equatorial emission model with two sets of (θ_M, a). The first was set to the average values from the joint posteriors, $(\theta_M, a) = (4.32 \ \mu\text{as}, 0.63)$. The second was to set to $(\theta_M, a) = (4.2 \ \mu\text{as}, 0.0)$, exploring the posterior associated with a truth value of zero spin. These are

shown in Figure 9 by the dashed red and green lines, respectively, in the one-dimensional, marginalized posteriors for θ_M and a. Both exhibit the same posterior excess near $a = 1$, implying that it is not significant.

5.4. Synthesis and Discussion

The accuracy of previous EHT estimates of θ_M for M87* is dominated by systematic uncertainties associated with the astrophysics of the emission region (Paper VI; Gralla et al. 2019). However, the detection of the bright ring reduces a number of these uncertainties, both qualitatively and quantitatively.

The mass estimate presented in Section 5.1, in which the bright ring is identified with the $n = 1$ photon ring, is independent of even pathological near-equatorial emission distributions. As a result, the direct detection of the bright ring has effectively produced a mass estimate in which the impacts of astrophysical uncertainties are strictly bounded. While the systematic uncertainty associated with this detection is nearly twice that reported in Paper VI, it is no longer dependent on the astrophysical calibration procedure used there, eliminating a key astrophysical uncertainty.

The combined image reconstructions confirm that the image morphology on each day is similar to those produced by GRMHD simulations, comprised of a bright ring and a diffuse, more variable surrounding emission structure. This provides a
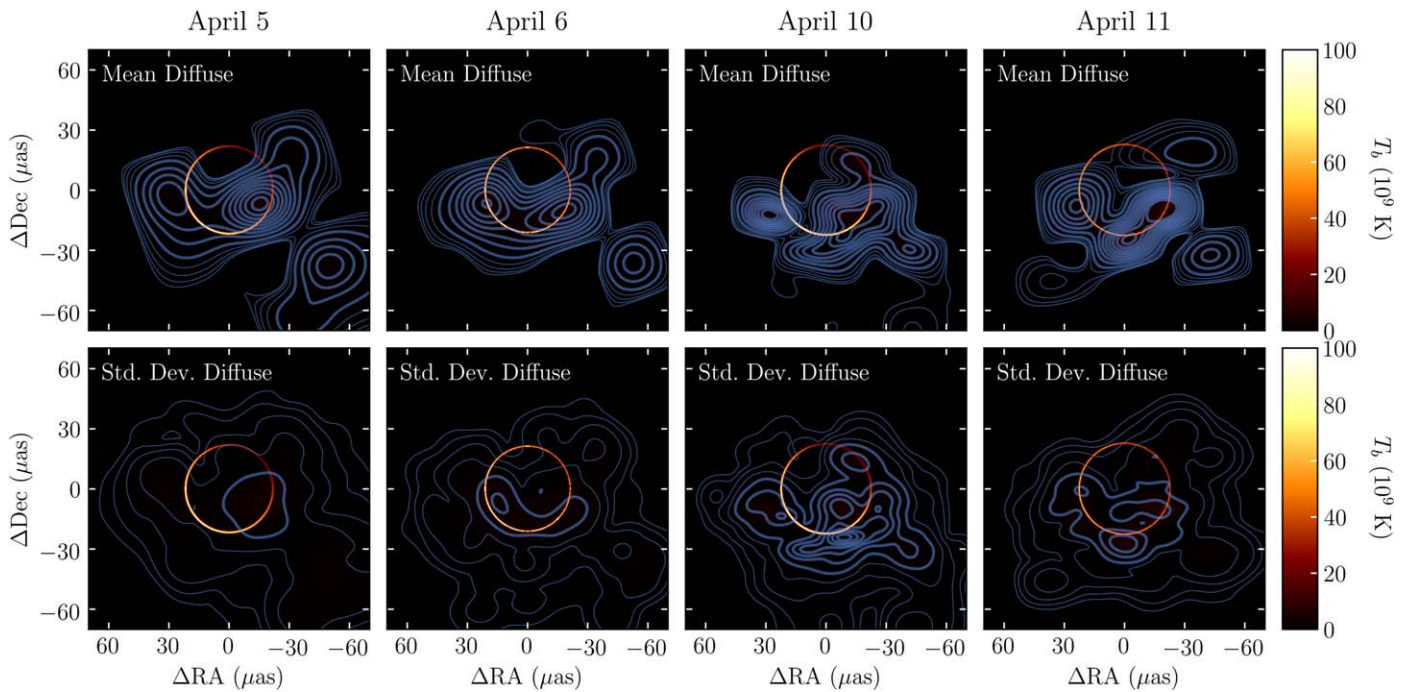
Figure 5. Brightness temperature maps of M87 on each day with fitted slashed ring (color scale) separated from the average (top) and standard deviation (bottom) of the reconstructions of the more diffuse background image (contours) produced from 10^4 samples drawn from the posterior. The ring color scale is linear and the ring flux map is smoothed with a circular beam with a FWHM of 0.5 μas. The background emission is shown in contours—thin contours are located at (0.25, 0.5, 1, 2) $\times 10^8$ K, thick contours are linearly spaced beginning at 4×10^8 K in steps of 4×10^8 K—and smoothed with a circular beam with a FWHM of 15 μas.

strong conceptual foundation for the calibrated mass estimates using GRMHD simulations presented in Paper VI and revised in Section 5.2. The inclusion of a prior expectation on the size of the emission region, inherent in the GRMHD simulations, results in significant improvements of systematic uncertainties. As a result, the effective systematic uncertainty is reduced to roughly half of that in Paper VI.

Finally, the diffuse emission provides a direct, astrophysics-independent estimate of the emission region location. Joint modeling of the bright ring and the diffuse component as the $n = 1$ and $n = 0$ photon rings, respectively, generates an astrophysics-independent estimate of the mass that incorporates the remaining systematic uncertainties directly as statistical errors. The half-range is approximately a quarter of that quoted in Paper VI. This implies that the position of the $n = 0$ photon ring provides a stronger constraint on the location of the emission region than the prior inferred from the GRMHD simulations from Paper V.

All of the mass estimates presented here are consistent among each other within their respective systematic errors. They are also consistent with the combined mass estimates presented in Paper VI, though they lie at the high end of the mass range listed there. This suggests that those GRMHD simulations with more compact emission regions are more consistent with the diffuse emission maps reconstructed here.

These mass estimates are also consistent with those arising at scales of 10^2 pc from the dynamics of stars (Gebhardt et al. 2011). It remains inconsistent with the gas dynamical mass estimate reported in Walsh et al. (2013). The significance of this discrepancy has now grown to more than 4σ. This inconsistency may be ameliorated by adjustments in the underlying gas disk model (Jeter et al. 2019; Jeter & Broderick 2021).

6. Origin and Evolution of the Diffuse Component

The detection of a bright ringlike feature, and its separation from the diffuse component, has a number of immediate implications for the origin of the emission and the properties of the central black hole. As shown explicitly in Broderick et al. (2020b), the morphology of the diffuse emission is accurately recovered despite the absorption of excess flux into the thin ring component. Thus, here we discuss the structure the diffuse component in the broader context of the environment and properties of M87*.

6.1. Evolution of M87 from 2017 April 5–11

There are clear signatures of evolution across the EHT observation campaign. The diffuse emission maps on neighboring days are similar. This is consistent with expectations based on the dynamical timescales; $GM/c^3 \approx 9$ hr in M87*, and GRMHD simulations indicate little evolution on timescales shorter than $10GM/c^3$ (Porth et al. 2019).

In contrast, significant evolution in the diffuse emission occurs between the first two days (April 5, 6) and the last two days (April 10, 11). This evolution seems to primarily manifest as the addition in the later two days of a distinct component to the southern region of the diffuse ring. The absence of an intervening observation leaves the origin of this southern component unclear; it could be a new component appearing, or it could be a growing extension of the western component. The latter interpretation would be consistent with the clockwise rotation of the black hole inferred from the orientation of the diffuse ring (Paper IV) and possibly to outflowing features within the jet (Jeter et al. 2020). Note that the sense of this rotation is opposite to the predominantly counterclockwise evolution identified in the total emission map, exhibited in Figures 2 and 4, as well as other analyses (Paper IV; Arras et al. 2022; Carilli & Thyagarajan 2022).

Table 2
Hybrid Image-ring Fit Parameters

Day	$I_{\rm diff}$ (Jy)	$\theta_{\rm diff}$ (μas)	$I_{\rm ring}$ (Jy)	$\theta_{\rm ring}$ (μas)
April 5	$0.252^{+0.019+0.045}_{-0.017-0.044}$	$17.0^{+1.1+3.4}_{-1.2-2.6}$	$0.301^{+0.007+0.022}_{-0.007-0.017}$	$21.88^{+0.13+0.36}_{-0.14-0.37}$
April 6	$0.190^{+0.014+0.037}_{-0.012-0.041}$	$20.2^{+1.0+2.6}_{-1.3-5.2}$	$0.276^{+0.010+0.049}_{-0.008-0.019}$	$21.44^{+0.09+0.21}_{-0.10-0.23}$
April 10	$0.176^{+0.017+0.047}_{-0.019-0.052}$	$20.4^{+4.2+7.0}_{-4.7-6.7}$	$0.302^{+0.016+0.038}_{-0.021-0.054}$	$21.89^{+0.27+0.51}_{-0.39-0.90}$
April 11	$0.193^{+0.013+0.035}_{-0.018-0.070}$	$20.8^{+0.7+2.8}_{-0.8-6.0}$	$0.246^{+0.020+0.058}_{-0.013-0.026}$	$22.51^{+0.16+0.37}_{-0.17-0.47}$

Note. Values quoted are the median, 50-, and 90-percentile ranges.
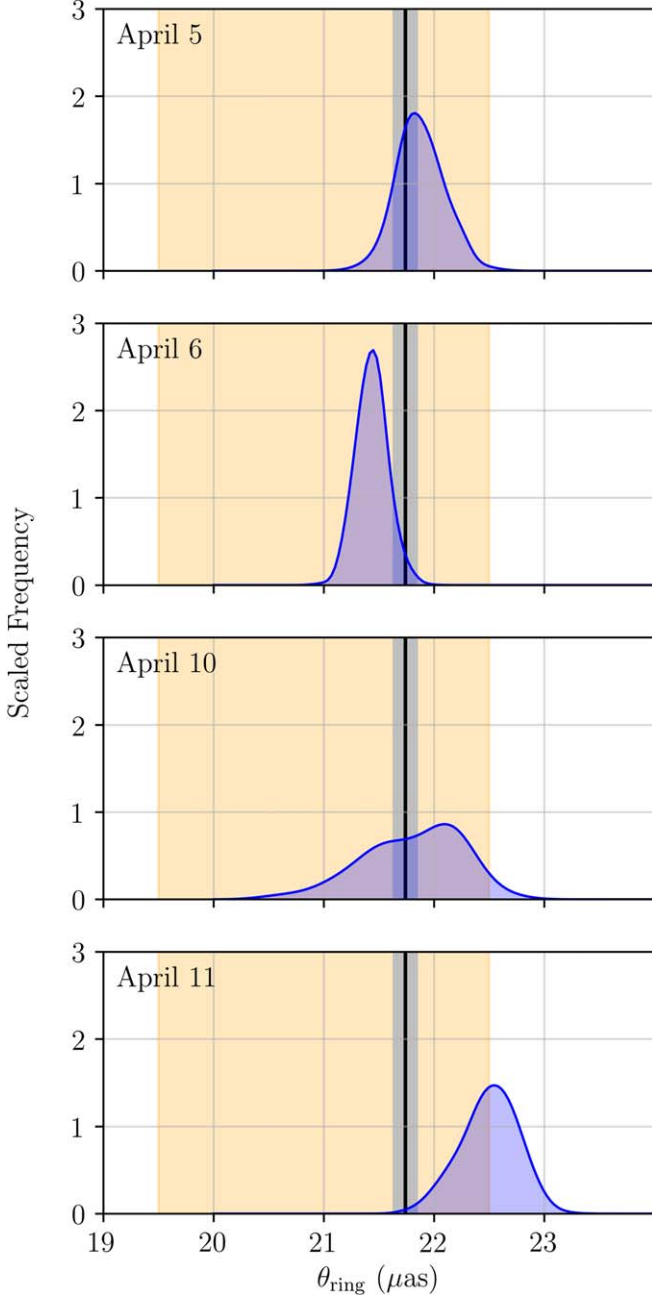
Figure 6. Posterior distributions for the radius of the thin ring component on each day. The variance-weighted estimates from all days and their uncertainties are indicated by the black vertical lines and gray bands, respectively. The range of ring diameters from Paper VI are indicated by the orange bands.

Figure 7. Absolute shift in the radius of the $n = 1$ photon ring (bottom) for a distant polar observer in comparison to the radius of the asymptotic photon ring ($n = \infty$) as functions of the apparent diameter of the direct image ($n = 0$). The orange region indicates the 1σ range of ring sizes implied by Paper VI, 42 ± 3 μas.

Table 3
M87* Mass Estimates

Method/Origin	θ_M (μas)	M (10^9 $M_\odot$)
§5.1 Direct $n = 1$ photon ring	4.15 ± 0.74	7.06 ± 1.26
§5.2 Corrected $n = \infty$ photon ring	4.22 ± 0.17	7.18 ± 0.29
§5.3 Joint M/a reconstruction	$4.20^{+0.12}_{-0.06}$	$7.13^{+0.20}_{-0.11}$
Paper VI	3.8 ± 0.4	6.5 ± 0.7
Gebhardt et al. (2011)	$3.62^{+0.60}_{-0.34}$	$6.14^{+1.07}_{-0.62}$
Walsh et al. (2013)	$2.05^{+0.48}_{-0.16}$	$3.45^{+0.85}_{-0.26}$

Note. Errors indicate 1σ statistical and systematic errors, added in quadrature. See the relevant sections for more detailed error budgets.

component are detected. This is consistent with the interpretation of this feature as primarily gravitational, and thus dependent only weakly on the details of the otherwise evolving emission region.

Equally important, if not more so, is what does *not* evolve. No significant changes in the angular size of the narrow ring

6.2. Extended Southwestern Emission

In all of the diffuse emission maps shown in Figure 5, an extension to the southwest is visible. The ability to produce a statistically meaningful image posterior enables the assignment
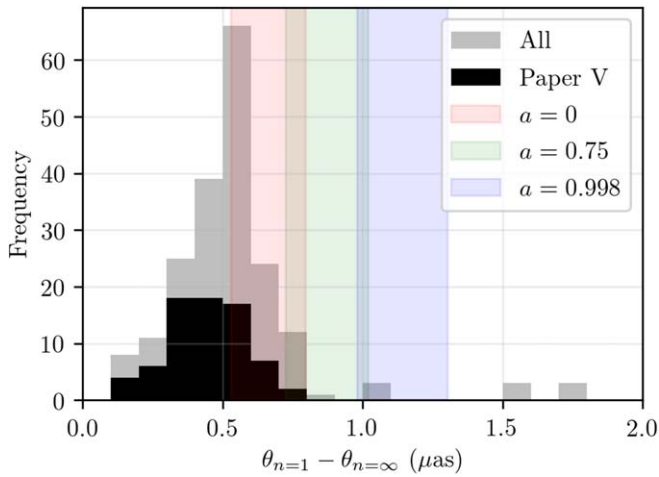
Figure 8. Absolute shift in the radius of the $n = 1$ photon ring relative to the radius of the asymptotic ($n = \infty$) photon ring from the GRMHD simulation library presented in Paper V, where we have identified the $n = 1$ ring with the bright ringlike feature seen in the GRMHD images. The distribution of all models (including those excluded in Paper V) is shown in gray and those models that are not excluded by the 2017 EHT observations in black. The ranges inferred from the geometric arguments, assuming emission from only the equatorial plane and using the size constraint from Paper VI, are shown by the vertical ranges for $a = 0$ (red), $a = 0.75$ (green), and $a = 0.998$ (blue).
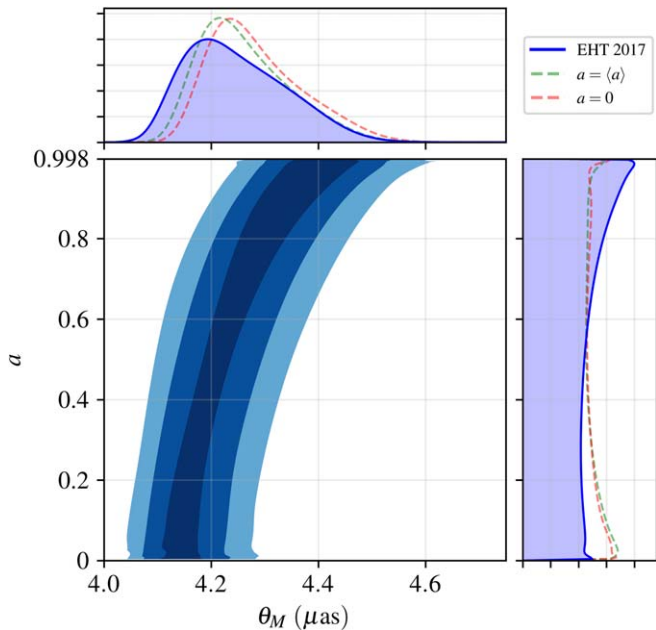
Figure 9. Joint posterior on the spin and mass of M87* from the measurements of $\theta_{n=0}$ and $\theta_{n=1}$ across the four observation days in the 2017 EHT campaign. Contours indicate cumulative 50%, 90%, and 99% regions. For comparison, the one-dimensional marginalized posteriors on M and a are shown by the dashed lines for simulated ring sizes generated, assuming a single emission radius and Gaussian errors with the sizes quoted in Table 2.

of a significance to these features, which ranges from 4σ to 12σ on the individual days. On three of the four days there is a matching northwestern extension, though this is less significant (1σ–2σ).

While such features appear similar to the dirty beams seen in some M87* images produced by other algorithms (see Figures 7 and 8 of Paper IV), none have been seen at statistically significant levels (as characterized by the image posteriors) in

the various simulated data tests performed with the Bayesian scheme employed here (see, e.g., Figure 4 of Broderick et al. 2020b). Similar claims of a statistically significant detection have been made by other groups (Arras et al. 2022; Carilli & Thyagarajan 2022).

It is suggestive that the orientation of these diffuse extensions align with the limb-brightened jet seen at 3 mm, shown in Figure 10. We align the center of light of the mean 1.3 mm maps, averaged over the four observation days in 2017, and the centroid of the core component of the 3 mm maps. The ridgeline fits from Kim et al. (2018) are also shown in Figure 10, assuming a jet position angle of 69° east of north and a width, $W \propto z^{-0.498}$, where z is the projected core distance. Additional core shifts along the jet of 25 μas and transverse to the jet of $-10\,\mu$as are applied. Extrapolating the core shift power law determined from longer wavelengths by Hada et al. (2011) places the anticipated 1.3 mm core on top of the brightest diffuse component.[51] With these shifts, the ridgelines connect from the southwestern and northwestern extensions. We caution that the apparent structure of the jet base on horizon scales may depart substantially from the power-law behavior at large scales due to the combined effects of inclination, gravitation lensing at small radii, inhomogeneous evolution in the optical depth across the image, and relativistic motion (see, e.g., Broderick & Loeb 2009; Mościbrodzka et al. 2016; Chael et al. 2019; Davelaar et al. 2019).

The dominance of the southwestern extension, in comparison to the more marginal northwestern extension, is consistent with a rapidly rotating jet structure near the black hole, aligned with the black hole spin. Brightness temperature profiles are shown in Figure 11 along the corresponding paths shown in Figure 10. The brightness ratio between these two components reaches values as low as $\mathcal{R} \approx 0.2$ at similar projected distances from the black hole. The uncertainty of these profiles is a combination of the intrinsic uncertainty in the reconstructions and of the ridgelines themselves; we show the uncertainty associated with a Gaussian error in the position of the parabola apex (the rightmost open green point in Figure 10) of 2 μas for the EHT profiles and 10 μas for the 3 mm profiles.

In Figure 11 the difference in the brightness temperature profiles is naturally explained by black hole spin-driven jets like those first described in Blandford & Znajek (1977). Relativistic rotational motions in the emitting plasma near the black hole, with velocities that could reach as high as $c/2$, are a consequences of the twisted magnetic field lines that penetrate the horizon and extract the rotational energy of the black hole. These motions are seen explicitly in GRMHD simulations (see, e.g., Wong et al. 2021). At larger distances, this rotation is suppressed due to angular momentum conservation, at which point the jet plasma motions become predominantly poloidal. As a result, even only very modest increases in the jet height result in drastic reductions in the beaming-induced brightness asymmetry, naturally explaining its absence at 3 mm and longer wavelengths.

In both Figure 10 and Paper V the implied spin of the black hole is oriented into the sky, i.e., the black hole rotates

---

[51] The positions of the 1.3 mm and 3 mm cores are strongly correlated in the fits reported in Hada et al. (2011). Thus, the *relative* positions of the 1.3 mm and 3 mm cores is much better constrained than the absolute position of either in relation to the 7 mm core. We estimate the uncertainty in the location of the 1.3 mm core via Monte Carlo sampling of the power-law fit parameters reported in Hada et al. (2011), assuming independent Gaussian errors in the fit parameters.
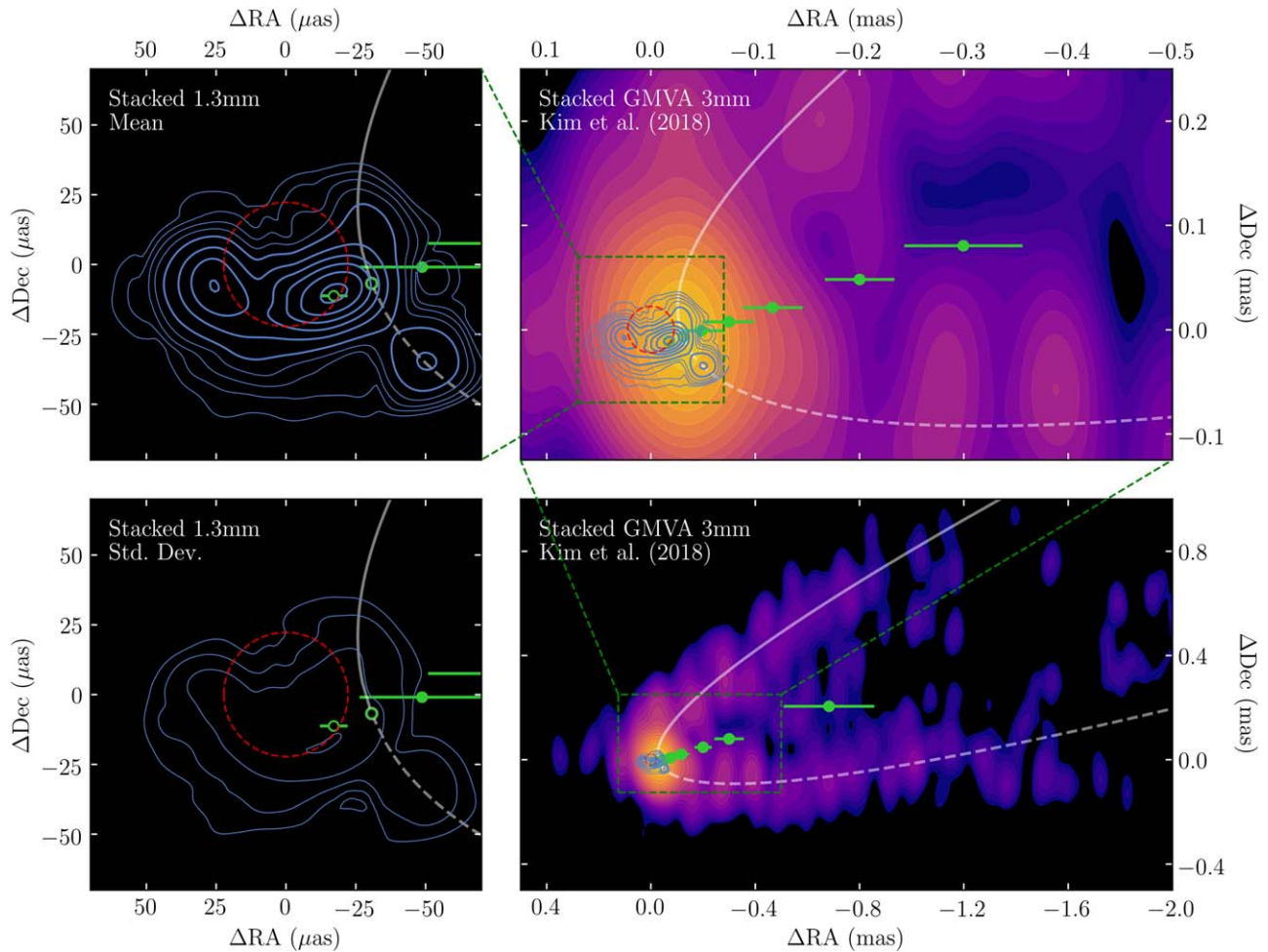
Figure 10. Comparison of the stacked image of the diffuse emission produced by the variance-weighted mean (upper left) and its standard deviation (lower left) with the stacked Global 3mm VLBI Array (GMVA) map at 3 mm from Kim et al. (2018; right). In the GMVA map, the extended jet is clearly visible, and the contours are located at $(-1, 1, 1.414, 2, \ldots) \times 0.47$ mJy beam^{-1}; the contours of the diffuse emission map are the same as in Figure 5. The fit to the ridgelines of the limb-brightened emission from Kim et al. (2018) are shown by white solid (top) and dashed (bottom) lines in each panel, with the origin shown by the open green circle. A ring with a mean radius of 22.22 μas is indicated by the dashed red line. Boundaries of neighboring panels are indicated in green dashed lines. Shown by green circles are the measured core shifts at 2.3 GHz (rightmost), 5, 8.4, 15.2, 23.8, and 43.2 GHz (leftmost closed) from Hada et al. (2011) referenced to the anticipated location of the 3 mm core (right open). The expected location of the 1.3 mm core (left open) matches the peak of the diffuse emission.

clockwise, dragging the emitting plasma with it. As such, this provides a striking, direct confirmation of black hole spin as the driver of the jet in M87*. In practice, the angular scale over which the limbs become symmetric depends on the detailed jet structure, and thus black hole spin (Takahashi et al. 2018); however, we leave further astrophysical interpretation to future work.

7. Conclusions

We have applied the hybrid imaging algorithm outlined in Broderick et al. (2020b) to the 2017 EHT observations of M87*. This method is a Bayesian imaging and modeling scheme that reconstructs the brightness map from visibility data, accounting for station gains and atmospheric phase delays, and produces statistically meaningful posteriors for both components. We considered both imaging and imaging with a narrow ring, finding that information criteria indicate a preference for the latter on three of four observation days.

We demonstrate that the EHT observations of the horizon scale emission of M87* support the presence of a narrow ringlike feature. Its radius is consistent across the seven days of

the 2017 EHT observing campaign (2017 April 5–11). The size and structure of this ring is consistent with the prominent lensed structure anticipated in horizon-resolving images of M87*. We associate the ring emission with the strong gravitational lensing that produces the $n = 1$ photon ring; this decomposition thus represents the first direct detection of the "back of the emission region." It also provides an important confirmation of the key role played by strong lensing in the formation of the images of M87* presented in Paper I.

Evolving, extended diffuse emission is clearly present in addition to the bright, narrow ring. The extended image is consistent among neighboring days, as anticipated by the long dynamical timescales in M87*. However, it differs from the beginning of the week to the end of the week. This may be due either to the appearance of a new southern component or the shearing of a western component southeastward. The latter is consistent with the direction of motion expected from the black hole spin orientation presented in Paper V.

The diffuse emission is dominated by compact components that surround the bright ring, similar to the morphology in many GRMHD simulation images. This is more compact than many such images, suggesting that additional constraints on the
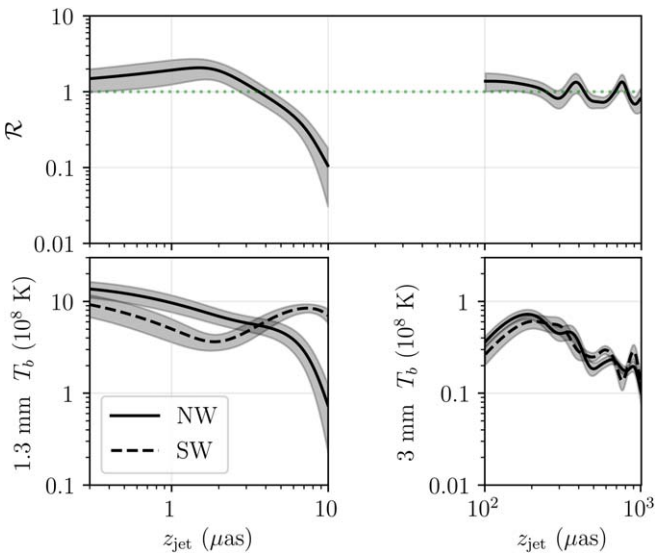
Figure 11. Bottom: flux profiles along the top and bottom jet ridgelines shown in Figure 10 for the stacked 1.3 and 3 mm emission maps. The latter have been smoothed over a scale of 100 μas to remove the clear beam features. The shaded regions indicate a combination of the intrinsic 1σ errors and that associated with nearby ridgelines. Top: implied brightness ratio between the two ridgelines. A brightness ratio of unity is shown by the green dotted line.

library in Paper V can be made based on the compactness of this portion of the diffuse emission.

Extended components within the diffuse emission are also detected at statistically significant levels. These include a southwestern extension, detected at between 4σ and 8σ across all days, and a northwestern extension that is only marginally detected on two days (April 5 and 11). Both of these components are reminiscent of the larger-scale limb-brightened features seen at 3 mm; their orientation matches those extrapolated from longer wavelengths. These may be tentatively identified with the rapidly rotating jet footprint. The difference in the luminosity of the southern and northern components would then be naturally explained by relativistic jet rotation at the jet base. Both of these would support the conclusion that the jet in M87* is driven by the black hole rotation, as described in Blandford & Znajek (1977).

The size of the bright ring and its relation to the diffuse emission presents a number of ways to estimate the black hole mass-to-distance ratio with varying degrees of astrophysical inputs. All of these estimates are consistent, with a $\theta_M = 4.15 \pm 0.74$ μas, independent of the extent of the emission region. Our most precise estimate arises from simultaneously reconstructing the ring and diffuse emission scales, and obtains $\theta_M = 4.20^{+0.12}_{-0.06}$ μas, which improves on the fractional uncertainty presented in Paper VI by a factor of more than four. The resulting mass estimate after folding in a distance of 16.8 Mpc is $7.13^{+0.20}_{-0.11} \times 10^9\,M_\odot$. The uncertainty in the mass estimate is now dominated by the systematic uncertainty in the distance of $0.35 \times 10^9\,M_\odot$.

These mass-to-distance ratio estimates are consistent with those from the variety of methods presented in Paper VI and from stellar dynamics (Gebhardt et al. 2011). Because the latter is estimated from the dynamics of what are effectively test particles at distances four orders of magnitude larger than the photon orbit, the comparison of these mass measurements provide a direct test of general relativity, as described in

Paper VI. In practice, this test remains limited by the uncertainty in the stellar dynamics measurement.

Nevertheless, the mass estimates presented here lie at the high end of the ranges presented in Paper VI. This suggests that the set of GRMHD simulations used to calibrate the mass estimates in Paper VI were more extended than the observed emission, biasing the calibration factor α toward high values and thus the mass toward low values. This is only partly ameliorated by selecting only MAD models in the calibration process. In comparison, no such calibration is required for two of the three mass estimates made here; in the one instance where calibration from simulations is performed, the measured systematic modification is small due to the much more robust size of the bright rings in simulated images.

Additional epochs of horizon-resolving observations will prove particularly useful in confirming the existence and nature of the bright ring. While small variations in its location are anticipated, associated with (potentially large) variations in the location of the emission region, if the ring structure detected here is, in fact, identified with the $n = 1$ photon ring, it should persist.

The evolution of the diffuse emission map will also be diagnostic of the location and origin of the emission in M87*. Similar quality observations that extend over observation epochs as short as two weeks will permit the conclusive differentiation between orbiting and outflowing features (Jeter et al. 2020). The ability to resolve dim, variable structures thus motivates longer-duration observing campaigns.

The constraints on black hole spin obtained here are inconclusive. However, the ability to constrain (θ_M, a) to a band in the mass-spin parameter space indicates that even a single, fortuitous future EHT observation of M87* may provide a measurement of black hole spin from gravitational lensing alone (Broderick et al. 2022). The strength of potential spin constraints depends on the degree to which the emission region location differs during future observations. Multiple additional measurements provides a lensing-only test of general relativity (Broderick et al. 2022). These provide a strong motivation for including M87* in future EHT campaigns and those of subsequent instruments.

It also suggests that future space-based millimeter-very long baseline interferometry experiments may be able to detect the next-order lensed image, i.e., that associated with the $n = 2$ ring, via a similar method to that presented here (Broderick et al. 2022). The astrophysics-independent mass measurements become substantially better constrained in this instance, and immediate tests of general relativity become possible.

Finally, this provides a direct demonstration of the ability to leverage high S/N data to estimate image features with precisions that significantly exceed those implied by the ostensible observing beam. This effective super-resolution may suggest that a similar effort applied to more distant sources may yield practical mass estimates even in the absence of resolved ring structures in images.

Appendix A
Model Components and Priors

We employ three model components in the comparisons made here. These are the "nonparameteric" raster splined raster model, the large-scale Gaussian, and a slashed crescent. Here we collect details of the implementation and assumed priors on each component.

The splined raster model is described in Broderick et al. (2020b), to which we direct the reader for more detailed information. It is characterized by a rectilinear set of control points, $I_{M,N}$, which may vary independently. An example with the control points explicitly marked is shown in Figure 12. The intensity map is interpolated between these control points using an approximate cubic spline. We modify this by permitting a variable field of view, $(\text{FOV}_x, \text{FOV}_y)$, orientation, ϕ, and shift in the center of the raster, (x, y). Parameters and priors are listed in Table 4. Note that the ring radius in angular units is given by $\theta = R(1 - \psi/2)$.

The large-scale Gaussian is the asymmetric Gaussian model described in Broderick et al. (2020a). This is characterized by a total flux, I_0, a symmetrized standard deviation, σ, asymmetry parameter, A, position angle, ϕ, and location (x, y). Parameters and priors are also listed in Table 4.

Finally, we apply the slashed ring using the xs-ringauss model described in Broderick et al. (2020a). We force the asymmetry parameter and additional Gaussian to vanish via the choice of appropriate priors. This leaves the total flux, I_0, outer radius, R, fractional width, ψ, linear brightness gradient, f, brightness gradient position angle, PA, and location, (x, y). Of
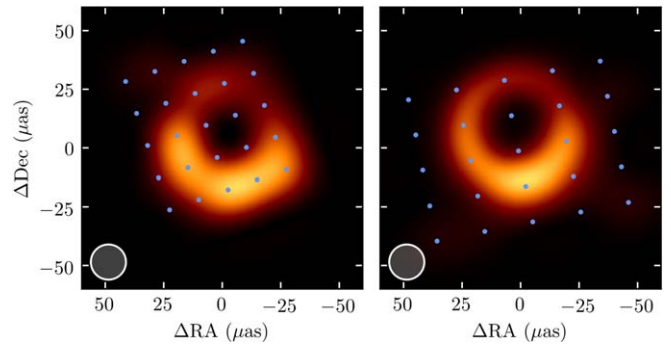

Figure 12. Illustration of the location of image raster control points for a representative $I_{5\times5}+A$ model (left) and $I_{5\times5}+A+X$ model (right). To facilitate direct comparisons between the intensity maps for the two models, both have been smoothed by a 15 μas Gaussian beam, shown in the lower left of each panel.

Table 4
Hybrid Image-ring Fit Priors

Comp.	Param.	Units	Prior[a]
Raster	$I_{M,N}$	Jy μas^{-2}	$\mathcal{L}(10^{-14}, 3 \times 10^3)$
$I_{M\times N}$	FOV_x	μas	$\mathcal{U}(0, 200)$
	FOV_y	μas	$\mathcal{U}(0, 200)$
	ϕ	rad	$\mathcal{U}(-0.25\pi, 0.25\pi)$
	x	μas	$\mathcal{U}(-40, 40)$
	y	μas	$\mathcal{U}(-40, 40)$
Gaussian	I_0	Jy	$\mathcal{U}(0, 10)$
A	σ	mas	$\mathcal{U}(0.1, 10^4)$
	A	…	$\mathcal{U}(0, 1)$
	ϕ	rad	$\mathcal{U}(0, \pi)$
	x	mas	$\mathcal{U}(-2, 2)$
	y	mas	$\mathcal{U}(-2, 2)$
Ring	I_0	Jy	$\mathcal{U}(0, 2)$
X	R	μas	$\mathcal{U}(0, 10^2)$
	ψ	…	$\mathcal{U}(0, 0.05)$
	f	…	$\mathcal{U}(0, 1)$
	ϕ	rad	$\mathcal{U}(-\pi, \pi)$
	x	μas	$\mathcal{U}(-40, 40)$
	y	μas	$\mathcal{U}(-40, 40)$

Note.
[a] Linear priors from a to b are represented by $\mathcal{U}(a, b)$, logarithmic priors from a to b are represented by $\mathcal{L}(a, b)$.

these, we restrict in particular the fractional width to ensure that the ring thickness remains well below the scale of the spacings within the splined raster.

These are supplemented with a model for the scan-specific complex station gains. The logarithmic amplitudes of the gains are assumed to have a Gaussian prior with width 20% for all stations except the Large Millimeter Telescope (LMT), for which we assume a prior with width 100%. The phases priors are flat and uninformative. The gain phases are trivially degenerate with an overall shift in the image location, and thus we remove two parameters from the total parameter count in Table 1.

The contribution of the individual model components are illustrated in Figure 13. The observed decomposition matches that anticipated by the GRMHD models explored in Broderick et al. (2020b). The large-scale Gaussian only impacts the
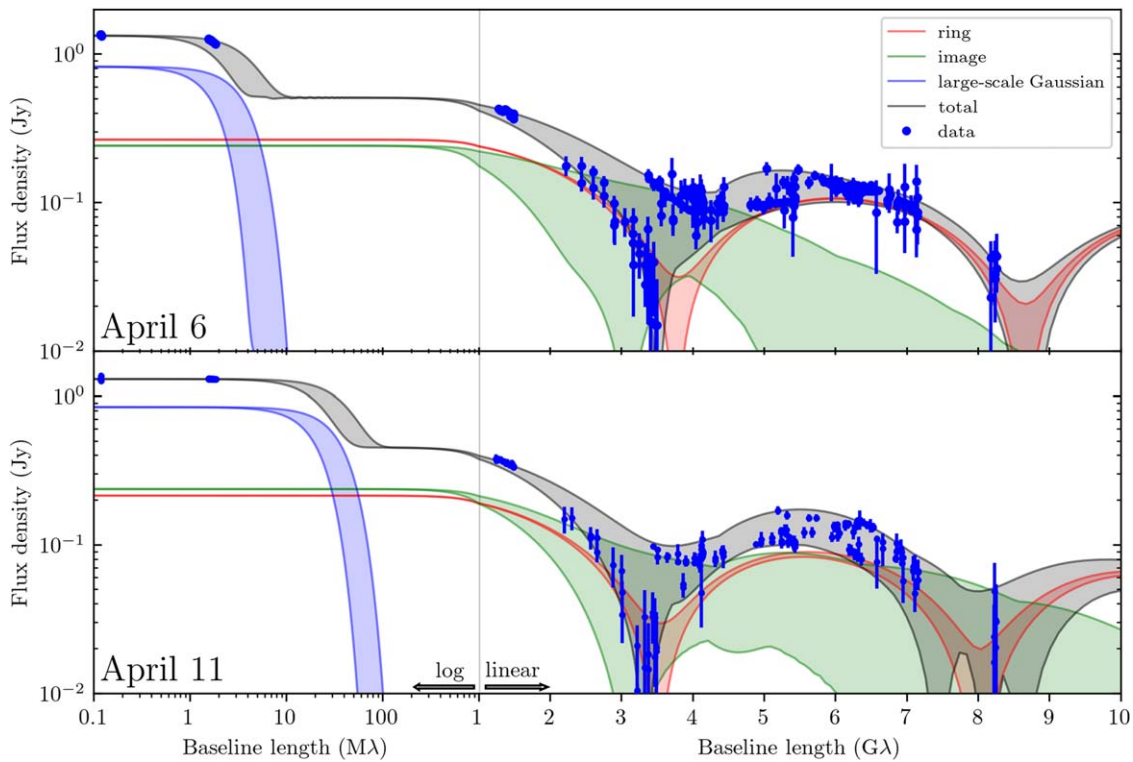
Figure 13. Visibility amplitude vs. baseline length for the April 6 (upper panel) and April 11 (lower panel) hybrid image model fits described in Section 4. In both panels, the colored bands show the range of amplitudes permitted for the ring component (red), the image component (green), the large-scale Gaussian component (blue), and their sum (gray). The gain-corrected data are plotted as blue points and error bars.
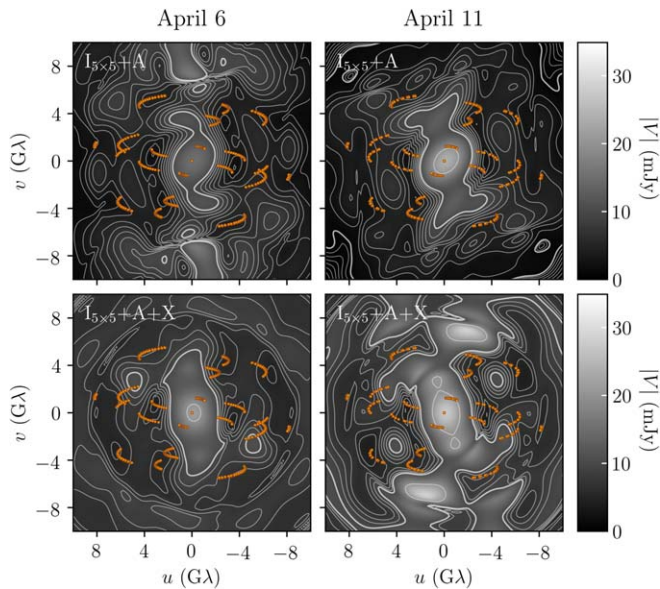

Figure 14. Posterior standard deviation maps of the visibility amplitudes on April 6 (left) and 11 (right) of the imaging reconstructions without (top) and with (bottom) a narrow ring component. Contours are logarithimic, with thick contours on powers of 10 and thin contours at intervening [2, 3, 4, 5, 6, 7, 8, 9]. (u,v) positions of the EHT data are shown in orange. The color range is linear with the magnitudes indicated by the color bars on the right.

intrasite baselines, the Atacama Large Millimeter/submillimeter Array (ALMA)-Atacama Pathfinder Experiment (APEX) telescope (APEX) and the James Clerk Maxwell Telescope (JCMT)-Submillimeter Array (SMA). The raster image and narrow ring both contribute at longer baselines, with the latter dominating at the longest baselines. The null in the visibility

amplitudes near $3.5\,\mathrm{G}\lambda$ is reconstructed by a combination of these components, both of which exhibit nulls shifted from the observed baseline length. In practice, Figure 13 shows the range of the visibility amplitudes at each baseline length, and thus the distinguishing power of the data exceeds that illustrated in Figure 13.

The result of the image-reconstruction process is a posterior distribution of brightness maps, corresponding to the posterior distribution of the underlying model parameters. As shown in Figure 14 for representative days, the posterior range of visibility amplitudes associated with the image posterior is small at (u,v) positions near the EHT measurements and largest in the (u,v) holes, prominently in the north/south near $4\,\mathrm{G}\lambda$. Thus, as expected, the posterior encompasses the uncertainty associated with the unknown visibilities away from the locations of the EHT data, subject to the constraints of the underlying image model.

Appendix B
Ancillary Fit Results

In addition to the diameter of the bright ringlike feature, a number of additional model parameters are constrained. In Figure 15 we collect some of the parameter constraints that may be of interest.

The ring flux posteriors present the same information reported in Table 2 and associated discussion, to which we direct the reader for more information.

The ring position angle estimates are consistent among days, in contrast to the reconstructions in Paper IV and Paper VI, which exhibited an evolution from April 5 and 6 to 10 and 11. The latter change is indicated in the second column of Figure 15 by the orange shaded region. In our analysis, this
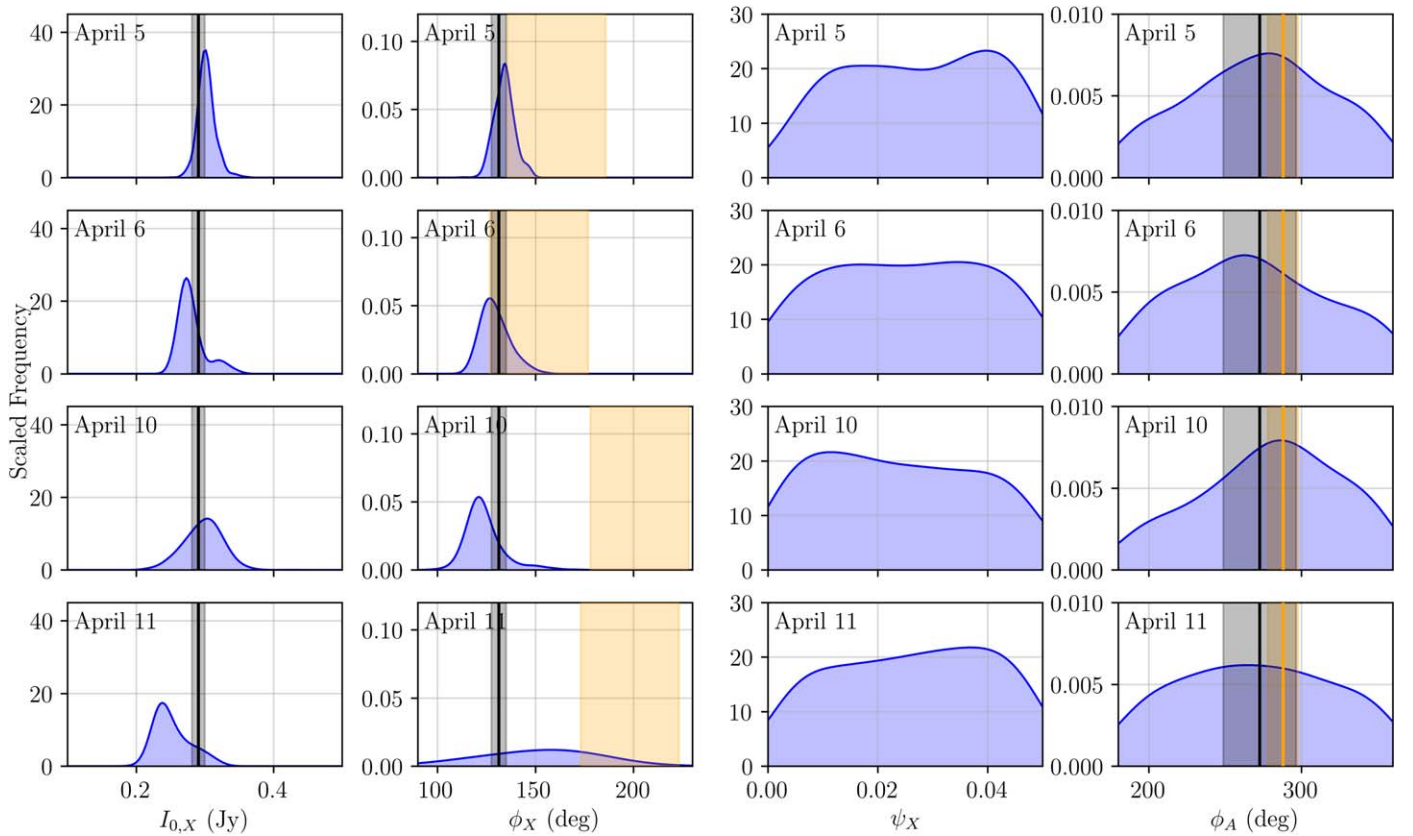
Figure 15. Posterior distributions for the ring flux, position angle, fractional width (ψ), and position angle of the large-scale Gaussian major axis. For the ring flux, ring positional angle, and Gaussian position angle, the black band indicates the combined 1σ estimate. The orange bands in the ring position angle posteriors show the range of permitted values from the THEMIS HI+LO xs-ringauss fits reported in Table 3 of Paper III. The orange bands in the Gaussian position angle posteriors indicate the orientation of the large-scale radio jet in M87*, with a $\pm10°$ range, consistent with the degree of jet precession observed. The width posterior is indistinguishable from the prior (see Table 4).

variation is entirely confined to evolution within the reconstructed diffuse emission.

The ring fractional width, ψ, fills the posterior, indicating that we have no traction on the width itself.

The orientation of the large-scale Gaussian is weakly constrained by the two sets of intrasite baselines, ALMA-APEX and JCMT-SMA. The posterior of the major-axis position angle is shown in the rightmost column of Figure 15. These are only very weakly nonuniform, though do peak in the octant consistent with the orientation of the large-scale radio jet. We do not attempt to interpret the large-scale Gaussian component further.

Appendix C
$n = 1$ Ring Bias Estimation

Generally, the $n = 1$ photon ring is biased relative to the asymptotic $n = \infty$ photon ring, associated with the boundary of the "shadow." To estimate the magnitude of this bias and its sensitivity to astrophysical uncertainties we explore both general geometric arguments and GRMHD modeling of M87* as described in Paper V.

C.1. Geometric Modeling

As described in Broderick et al. (2020b), the size of the emission region places a constraint on the magnitude of the difference between the $n = 1$ and $n = \infty$ photon rings. We

compute this here by explicitly tracing rays back toward the black hole launched from a polar observer and categorize trajectories by the number of equatorial plane crossings. Relevant examples are shown in Figure 16.

The diameter of the observed bright ring of 42 ± 3 reported in Paper VI places a limit on the location of an equatorial emission region. Assuming that this emission is dominated by the direct (i.e., $n = 0$) photon trajectories, this mapping may be made explicit. The population of orbits that terminate within the observed ring diameter is shown by the $n = 0$ range in each panel of Figure 16, and the region where they cross the equatorial plane is indicated by the thick bright line segments.

The $n = 1$ photon ring is then formed by those photon trajectories that intersect this portion of the equatorial plane after executing an additional half-orbit about the black hole. These may be traced forward to obtain the radial position on the image plane to which these trajectories contribute, $\theta_{n=1}$. These are also shown by the $n = 1$ range in each panel of Figure 16. A similar range of trajectories for $n = 2$ is shown for completeness.

The $n = \infty$ envelope is also computed, providing an estimate of the size of the photon ring, $\theta_{n=\infty}$. These may then be compared, yielding an estimate of the bias, $\theta_{n=1} - \theta_{n=\infty}$. These limits are summarized for a handful of black hole spins in Figure 7.

In practice, due to the finite resolution of the instrument, the diameter is weakly degenerate with the subbeam substructure
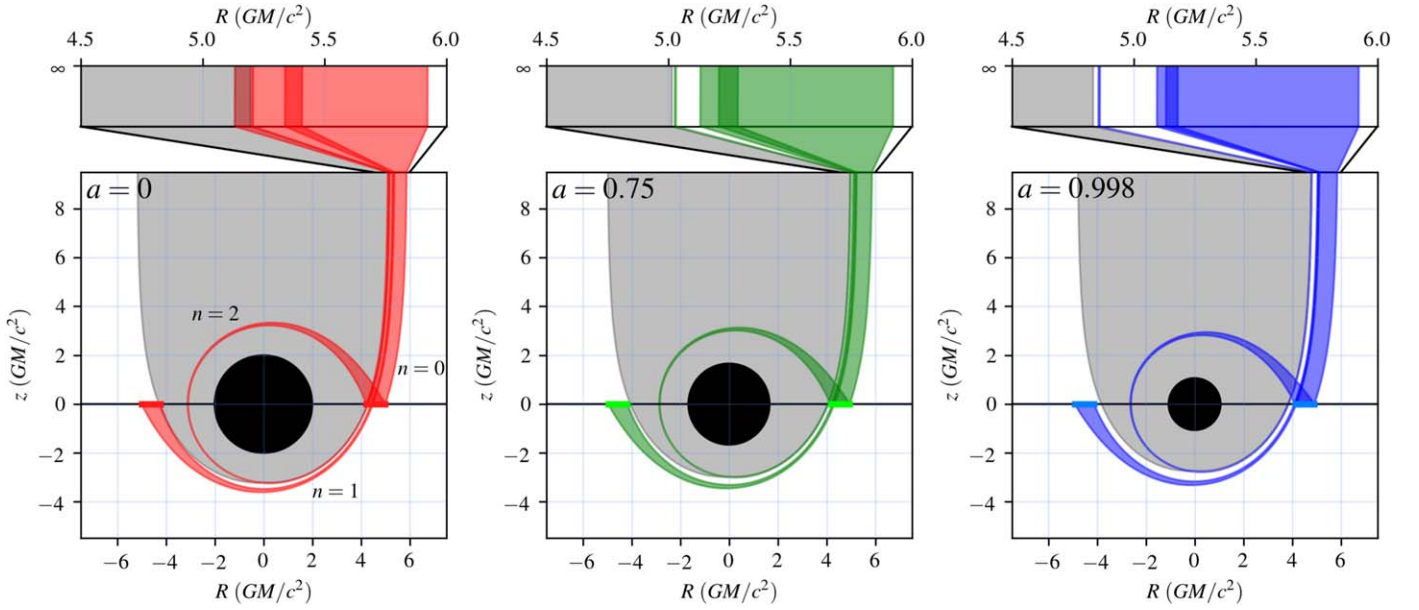
16

Figure 16. Photon orbits toward a polar observer, projected into the $R \equiv r \sin\theta \, \mathrm{sgn}\,\phi$ and $r\cos\theta$ plane, where r, θ, and ϕ are the normal Boyer–Lindquist coordinates and $\mathrm{sgn}\,\phi = \pm 1$ for $|\phi| < \pi/2$ and $|\phi| > \pi/2$, respectively. The region of the equatorial plane (thin black line) whose direct image ($n = 0$) is a ring with diameter $42 \pm 3 \ \mu$as is indicated by the thick bright line segment. The range of orbits that intersect this region for the direct emission ($n = 0$), after a half-orbit and thus contributing to the $n = 1$ photon ring, and after a full orbit and thus contributing to the $n = 2$ photon ring, are shown. The bar at the top shows a zoom in on the relevant side at $z = \infty$, and thus in the image plane. For reference, the gray region corresponds to the region within the "shadow," and the horizon is shown in black. Note that an empty region can exist between the $n = 0$ and $n = 2$ ring simply due to the emission distribution.
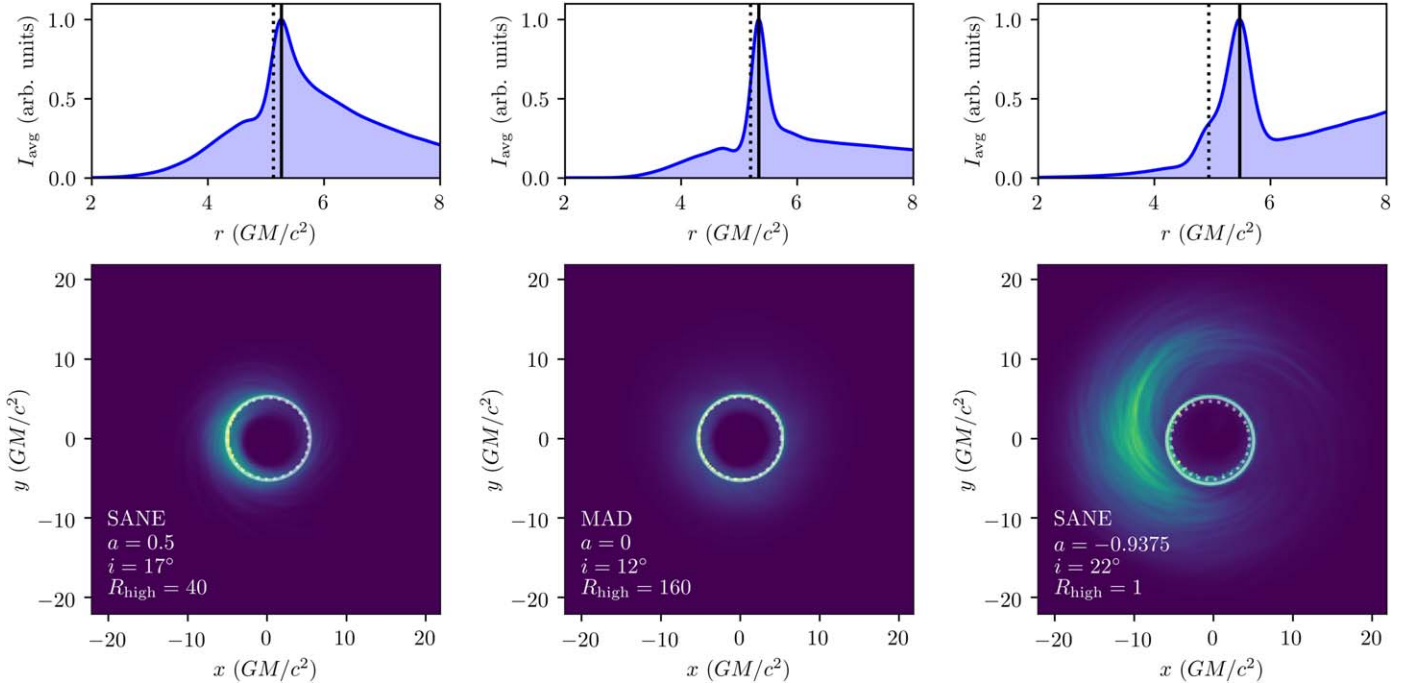

Figure 17. Example ring radius reconstructions for three simulations, chosen at random from those reported in Paper V. Bottom panels show average images from each simulation. In each, the semitransparent solid and dashed white circles indicate the best estimate of the bright ring location and the $n = \infty$ photon ring, respectively. Top panels show the corresponding azimuthally averaged, normalized radial flux profiles. The solid and dotted black lines indicate the best estimate of the bright ring location and the $n = \infty$ photon ring, respectively.

of the emission region. This manifests, for example, as a dependence on the width of the ring (see Appendix G of Paper IV). Therefore, these estimates of the range of the $n = 1$ photon ring bias are overestimates of the actual bias, and thus systematic uncertainty.

C.2. GRMHD Simulation

Because the bias between the $n = 1$ and $n = \infty$ photon ring radii depends on the emission distribution, we explored the relationship between the bright ring and the asymptotic photon

ring in GRMHD simulation images. We employed 198 GRMHD simulation image libraries, corresponding to those reported in Paper V supplemented by a set of $a = 0.75$ simulations. These span MAD and Standard and Normal Evolution (SANE) morphologies, $a \in [-0.9375, -0.5, 0, 0.5, 0.75, 0.9375]$, $i \in [12°, 17°, 22°]$, and $R_{\text{high}} \in [1, 10, 20, 40, 80, 160]$, where negative spins correspond to counterrotating accretion flows, R_{high} describes the relationship between the electron and ion temperatures, and the $a = 0.75$ simulations were performed only for the MAD morphology.

For each simulation, we time-averaged the simulated images to improve smoothness and reduce the impact of turbulent fluctuations. Generally, the image center will be shifted from the image origin, i.e., $(x, y) = (0, 0)$, as a result of the small nonzero inclinations and spin. Therefore, to determine the center we minimize the variance in the radial location of the image brightness maximum between $4GM/c^2$ and $7GM/c^2$. Finally, the brightness was computed along 36 radial chords originating from the image center, normalized by its maximum value between $2GM/c^2$ and $8GM/c^2$, and then averaged, generating I_{avg}. The radius of the bright ring was then taken to be the position of the peak of the I_{avg}. This procedure is shown for three examples in Figure 17.

Each time-averaged simulation image-ring fit was visually inspected; there are no significant failures. As anticipated by the geometric calculation in Appendix C.1, the outward bias in the location of the bright ring is dependent on the extent of the emission region, growing with the second moment of the image intensity map. The distribution of the shifts are shown in Figure 8 when the results for all simulations are included and when only those that were deemed acceptable in Paper V.

Appendix D
Joint Mass-spin Constraint Analysis

Following Broderick et al. (2022), we model the position of the peak of the $n = 0$ and $n = 1$ photon rings. The angular radii of the former are determined relative to the center of the fitted ring. These are listed in Table 2.

From these measurements, we construct a Gaussian log-likelihood from the measurements listed in Table 2:

$$\mathcal{L}(\theta_M, a, r_{\text{em},5}, r_{\text{em},6}, r_{\text{em},10}, r_{\text{em},11})$$
$$= \sum_{d=\text{day}} \sum_{m=0,1} \frac{[\theta_{n=m,d} - \vartheta_{n=m}(a, r_{\text{em,d}}, i)\theta_M]^2}{2\sigma^2_{n=m,d}}. \quad (D1)$$

The six parameters are the mass, spin, and the four radii at which the emission peaks on each day. In all cases we assume a polar observer ($i = 0$); due to the weak dependence of the $n = 0$ and $n = 1$ photon rings on inclination near the pole and the large uncertainties on the measured ring radii, this makes a small difference. The uncertainties $\sigma_{n=0,d}$ and $\sigma_{n=1,d}$ are computed directly from the standard deviations of the $\theta_{n=0}$ and $\theta_{n=1}$ estimates.

Priors on all parameters are adopted either on ranges large in comparison to their reconstructed values or (for spin) that encompass all physical values. Uniform priors are adopted on the mass and spin within the intervals $[0, 10\,\mu\text{as}]$ and $[0, 1]$, respectively. Logarithmic priors are adopted for each $r_{\text{em,d}}$ on the interval $[r_h, 25r_h]$, where $r_h = 1 + \sqrt{1 - a^2}$ is the horizon radius in units of GM/c^2.

We sample the corresponding posterior using the ensemble MCMC method provided by the emcee python package (Foreman-Mackey et al. 2013). We employ 64 independent walkers and run for 10^5 steps, discarding the first half of each chain. Explorations with simulated data sets and inspection of the resulting MCMC chains indicate that by this time they are well converged.

ORCID iDs

Avery E. Broderick ⓘ https://orcid.org/0000-0002-3351-760X
Dominic W. Pesce ⓘ https://orcid.org/0000-0002-5278-9221
Roman Gold ⓘ https://orcid.org/0000-0003-2492-1966
Paul Tiede ⓘ https://orcid.org/0000-0003-3826-5648
Hung-Yi Pu ⓘ https://orcid.org/0000-0001-9270-8812
Richard Anantua ⓘ https://orcid.org/0000-0003-3457-7660
Silke Britzen ⓘ https://orcid.org/0000-0001-9240-6734
Chiara Ceccobello ⓘ https://orcid.org/0000-0002-4767-9925
Koushik Chatterjee ⓘ https://orcid.org/0000-0002-2825-3590
Nicholas S. Conroy ⓘ https://orcid.org/0000-0003-2886-2377
Geoffrey B. Crew ⓘ https://orcid.org/0000-0002-2079-3189
Alejandro Cruz-Osorio ⓘ https://orcid.org/0000-0002-3945-6342
Yuzhu Cui (崔玉竹) ⓘ https://orcid.org/0000-0001-6311-4345
Sheperd S. Doeleman ⓘ https://orcid.org/0000-0002-9031-0904
Razieh Emami ⓘ https://orcid.org/0000-0002-2791-5011
Joseph Farah ⓘ https://orcid.org/0000-0003-4914-5625
Christian M. Fromm ⓘ https://orcid.org/0000-0002-1827-1656
Peter Galison ⓘ https://orcid.org/0000-0002-6429-3872
Boris Georgiev ⓘ https://orcid.org/0000-0002-3586-6424
Luis C. Ho
(何子山) ⓘ https://orcid.org/0000-0001-6947-5846
David J. James ⓘ https://orcid.org/0000-0001-5160-4486
Britton Jeter ⓘ https://orcid.org/0000-0003-2847-1712
Alejandra Jimenez-Rosales ⓘ https://orcid.org/0000-0002-2662-3754
Jun Yi Koay ⓘ https://orcid.org/0000-0002-7029-6658
Carsten Kramer ⓘ https://orcid.org/0000-0002-4908-4925
Thomas P. Krichbaum ⓘ https://orcid.org/0000-0002-4892-9586
Sang-Sung Lee ⓘ https://orcid.org/0000-0002-6269-594X
Michael Lindqvist ⓘ https://orcid.org/0000-0002-3669-0715
Iván Martí-Vidal ⓘ https://orcid.org/0000-0003-3708-9611
Karl M. Menten ⓘ https://orcid.org/0000-0001-6459-0669
Yosuke Mizuno ⓘ https://orcid.org/0000-0002-8131-6730
James M. Moran ⓘ https://orcid.org/0000-0002-3882-4414
Monika Moscibrodzka ⓘ https://orcid.org/0000-0002-4661-6332
Joey Neilsen ⓘ https://orcid.org/0000-0002-8247-786X
Chunchong Ni ⓘ https://orcid.org/0000-0003-1361-5699
Jongho Park ⓘ https://orcid.org/0000-0001-6558-9053
Luciano Rezzolla ⓘ https://orcid.org/0000-0002-1330-7103
Angelo Ricarte ⓘ https://orcid.org/0000-0001-5287-0452
Bart Ripperda ⓘ https://orcid.org/0000-0002-7301-3908
Lijing Shao ⓘ https://orcid.org/0000-0002-1334-8853
Fumie Tazaki ⓘ https://orcid.org/0000-0003-0236-0600
Kenji Toma ⓘ https://orcid.org/0000-0002-7114-6010
Pablo Torne ⓘ https://orcid.org/0000-0001-8700-6058
Jonathan Weintroub ⓘ https://orcid.org/0000-0002-4603-5204

Maciek Wielgus ⓘ https://orcid.org/0000-0002-8635-4242
Feng Yuan (袁峰) ⓘ https://orcid.org/0000-0003-3564-6437
Shan-Shan Zhao ⓘ https://orcid.org/0000-0002-9774-3606
Shuo Zhang ⓘ https://orcid.org/0000-0002-2967-790X

References

Abramowicz, M. A., & Fragile, P. C. 2013, LRR, 16, 1
Arras, P., Frank, P., Haim, P., et al. 2022, NatAs, 6, 259
Arras, P., Frank, P., Leike, R., Westermann, R., & Enßlin, T. A. 2019, A&A, 627, A134
Bardeen, J. M. 1973, in Black Holes (Les Astres Occlus), ed. B. S. DeWitt & C. DeWitt (New York: Gordon and Breach), 215
Blandford, R. D., & Znajek, R. L. 1977, MNRAS, 179, 433
Broderick, A. E., Gold, R., Karami, M., et al. 2020a, ApJ, 897, 139
Broderick, A. E., Tiede, P., Pesce, D. W., & Gold, R. 2022, ApJ, 927, 6
Broderick, A. E., & Loeb, A. 2009, ApJL, 703, L104
Broderick, A. E., Pesce, D. W., Tiede, P., Pu, H.-Y., & Gold, R. 2020b, ApJ, 898, 9
Broderick, A. E., Fish, V. L., Johnson, M. D., et al. 2016, ApJ, 820, 137
Carilli, C. L., & Thyagarajan, N. 2022, ApJ, 924, 125
Carpenter, B., Gelman, A., Hoffman, M. D., et al. 2017, J. Stat. Softw., 76, 1
Chael, A., Narayan, R., & Johnson, M. D. 2019, MNRAS, 486, 2873
Davelaar, J., Olivares, H., Porth, O., et al. 2019, A&A, 632, A2
Event Horizon Telescope Collaboration et al. 2019a, ApJL, 875, L1
Event Horizon Telescope Collaboration et al. 2019b, ApJL, 875, L2
Event Horizon Telescope Collaboration et al. 2019c, ApJL, 875, L3
Event Horizon Telescope Collaboration et al. 2019d, ApJL, 875, L4
Event Horizon Telescope Collaboration et al. 2019e, ApJL, 875, L5
Event Horizon Telescope Collaboration et al. 2019f, ApJL, 875, L6
Foreman-Mackey, D., Hogg, D. W., Lang, D., & Goodman, J. 2013, PASP, 125, 306
Gammie, C. F., McKinney, J. C., & Tóth, G. 2003, ApJ, 589, 444
Gebhardt, K., Adams, J., Richstone, D., et al. 2011, ApJ, 729, 119
Gralla, S. E., Holz, D. E., & Wald, R. M. 2019, PhRvD, 100, 024018
Hada, K., Doi, A., Kino, M., et al. 2011, Natur, 477, 185
Jeter, B., & Broderick, A. E. 2021, ApJ, 908, 139
Jeter, B., Broderick, A. E., & Gold, R. 2020, MNRAS, 493, 5606
Jeter, B., Broderick, A. E., & McNamara, B. R. 2019, ApJ, 882, 82
Johnson, M. D., Lupsasca, A., Strominger, A., et al. 2020, SciA, 6, eaaz1310
Kim, J. Y., Krichbaum, T. P., Lu, R. S., et al. 2018, A&A, 616, A188
Mościbrodzka, M., Falcke, H., & Shiokawa, H. 2016, A&A, 586, A38
Pesce, D. 2021, AJ, 161, 178
Porth, O., Chatterjee, K., Narayan, R. & Event Horizon Telescope Collaboration 2019, ApJS, 243, 26
Sun, H., & Bouman, K. L. 2020, arXiv:2010.14462
Syed, S., Bouchard-Côté, A., Deligiannidis, G., & Doucet, A. 2019, arXiv:1905.02939
Takahashi, K., Toma, K., Kino, M., Nakamura, M., & Hada, K. 2018, ApJ, 868, 82
Thompson, A. R., Moran, J. M., & Swenson, G. W., Jr. 2017, Interferometry and Synthesis in Radio Astronomy (3rd edn.; Berlin: Springer) doi:10.1007/978-3-319-44431-4
Tiede, P. 2021, PhD thesis, University of Waterloo
Walker, R. C., Hardee, P. E., Davies, F. B., Ly, C., & Junor, W. 2018, ApJ, 855, 128
Walsh, J. L., Barth, A. J., Ho, L. C., & Sarzi, M. 2013, ApJ, 770, 86
Wong, G. N., Du, Y., Prather, B. S., & Gammie, C. F. 2021, ApJ, 914, 55